

A review on fundamentals for designing oxygen evolution electrocatalysts

Song, Jiajia; Wei, Chao; Huang, Zhen-Feng; Liu, Chuntai; Zeng, Lin; Wang, Xin; Xu, Zhichuan
Jason

2020

Song, J., Wei, C., Huang, Z., Liu, C., Zeng, L., Wang, X. & Xu, Z. J. (2020). A review on fundamentals for designing oxygen evolution electrocatalysts. *Chemical Society Reviews*, 49(7), 2196-2214. <https://dx.doi.org/10.1039/C9CS00607A>

<https://hdl.handle.net/10356/153346>

<https://doi.org/10.1039/C9CS00607A>

© 2020 The Royal Society of Chemistry. All rights reserved. This paper was published in *Chemical Society Reviews* and is made available with permission of The Royal Society of Chemistry.

Downloaded on 28 Aug 2022 04:59:27 SGT

A Review on Fundamentals for Designing Oxygen Evolution Electrocatalysts

Jiajia Song,^{a,b,c,*} Chao Wei,^{b,d,*} Zhen-Feng Huang,^e Chuntai Liu,^f Lin Zeng,^g Xin Wang,^e Zhichuan J. Xu,^{b,h*}

Electricity-driven water splitting is able to store electrical energy in the form of hydrogen gas. As a half-reaction of electricity-driven water splitting, the oxygen evolution reaction (OER) is the major bottleneck due to the sluggish kinetics of this four-electron reaction. Developing low-cost and robust OER catalysts is critical to solving the efficiency problem of water splitting. The catalyst design has to be built based on fundamental understandings of the OER mechanism and the origin of the reaction overpotential. In this article, we summarize the recent progress in understanding OER mechanisms, which include the conventional adsorbate evolution mechanism (AEM) and lattice oxygen-mediated mechanism (LOM) from both theory and experiment aspects. We start with the discussion on the AEM and its linked scaling relations among various reaction intermediates. The strategies to reduce overpotential based on the AEM and its derived descriptors are then introduced. To further reduce OER overpotential, it is necessary to break the scaling relation of HOO* and HO* intermediates in conventional AEM to go beyond the activity limitation of the volcano. The strategies including stabilization of HOO*, proton acceptor functionality, and switch of OER pathway with LOM, are discussed. The remaining questions on the OER and related perspectives are also presented at the end.

1. Introduction

Solar energy is one of the most abundant natural resources, but it suffers from an intermittent availability due to regional or seasonal factors. Converting solar into electrical energy by, for example, solar cells, is one of the promising methods to make use of it, but it is difficult to store the excess of electricity in large-scale by battery.¹⁻⁴ Storing the excessive amount of electrical energy in the forms of chemical bonds, such as H₂, by electricity-driven water splitting is another promising strategy,^{1, 5-7} because H₂ can store greater energy per unit weight or volume due to its high energy density, providing large-scale and uninterrupted energy storage. The electrical energy can be subsequently regenerated by fuel cells with a low level of pollution. In addition, H₂ also can be used as a feedstock in chemical industry processes to synthesize high value-added chemicals material.^{2, 8, 9}

The electricity-driven water splitting is composed of two half-cell reactions, which are separated by a membrane (Fig. 1).¹⁰ The reduction process at the cathode, i.e. $2\text{H}^+ + 2\text{e}^- \rightarrow \text{H}_2$, is hydrogen evolution reaction (HER), and the oxidation process at the anode, i.e. $2\text{H}_2\text{O} \rightarrow \text{O}_2 + 4\text{H}^+ + 4\text{e}^-$, is oxygen evolution reaction (OER). Compared with HER, OER is more kinetically sluggish because OER is a four-electron transferred reaction, while HER needs only two electrons. Thus, OER is the key process that governs the overall efficiency of electrochemical water splitting. To date, IrO₂ and RuO₂ are the state-of-the-art OER catalysts.¹⁰⁻¹⁴ However, both of them are made of precious metals and the cost is high. Therefore, it is imperative to seek for low-cost alternative materials that can effectively reduce the kinetic limitation of OER and improve the efficiency of water splitting.¹⁵⁻¹⁸

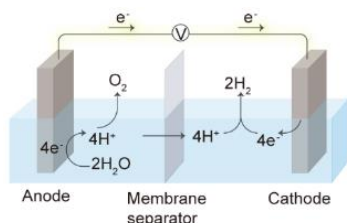


Fig. 1 Schematic illustration of electrocatalytic water splitting.

The OER performance of an electrocatalyst depends on the number of active sites and the activity of the active site (the latter is often defined as the intrinsic activity of the catalyst).^{11, 19-21} For the former aspect, increasing the exposure of electrochemically active sites by reducing the particle size,^{13, 22} engineering catalyst morphology,²³⁻³³ and promoting surface reconstruction of catalysts into the active species,³⁴⁻⁴⁴ have been widely reported. For the latter aspect, improving the activity of the active site that enables OER at potentials close to the thermodynamic limit requires researchers to fundamentally understand the reaction mechanisms and find the origin of the reaction overpotential at the active site of different materials. Note that, in recent decades, researchers have developed several reaction mechanisms. With the guide of those discovered mechanisms, it is possible to design more efficient OER electrocatalysts.

In this review, we focus on the recent progress in understanding OER mechanisms with related experimental evidence and summarize the established guidelines for OER electrocatalyst design. First, the conventional adsorbate evolution mechanism (AEM) and its scaling relations between different reaction intermediates are discussed. The strategies of improving the intrinsic activity based on the AEM and its derived popular descriptors are introduced. Although scaling relation in AEM can help screen catalyst quickly, it gives rise to a limitation for the OER activity. Second, the strategies of bypassing the limitation of AEM, including stabilizing the intermediate HOO*, functionalizing the proton acceptor, and even enabling the lattice oxygen-mediated mechanism (LOM), are summarized. In the last section, we discuss the remaining questions and challenges, and provide some proposed topics that are potentially interesting for future research.

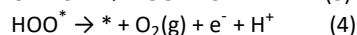
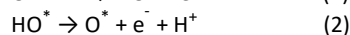
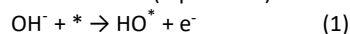
2. Design efficient OER catalysts based on AEM and its scaling relation

It is widely accepted that OER can proceed through two different mechanisms: AEM and LOM. As the covalency increases, the ability of metal cations to bind with oxygen becomes weak, and direct O-O bonding with reversible formation of oxygen vacancy (LOM) may become favorable. This LOM mechanism will be detailed in the part

of “lattice oxygen-mediated mechanism (LOM)”. In this section, we mainly focus on the former by analyzing the adsorption-energy scaling relation, activity volcano plot and descriptor.

2.1 AEM and its related scaling relation

The AEM is typically assumed to involve four concerted proton-electron transfer (CPET) reactions centered on metal ion, as described in Equations (1-4).⁴⁵⁻⁴⁷ At each step, a proton is injected into the electrolyte, eventually combining with a transferred electron at the cathode. Specifically, OH⁻ first adsorbs on the surface O vacancy site (Equation 1). The adsorbed OH (HO* species) then undergoes subsequent deprotonation to form O* (Equation 2). The following O-O bond formation step allows O* to react with another OH⁻ to form the HOO* intermediate (Equation 3). In the final step, O₂ is evolved through deprotonation of HOO* with the regeneration of the active site (Equation 4).



Using standard hydrogen electrode (SHE) as the reference potential, the chemical potential of H⁺ + e⁻ is equal to that of 1/2 H₂ in the gas phase. Applying an external bias (*U*) on the PCET processes in Equations (1-4) needs to add a -*eU* term in their reaction free energies. The theoretical overpotential referring to reversible hydrogen electrode (RHE) doesn't depend on the pH because free energies vary with pH and *U* in the same way.^{48, 49} Therefore, the reaction free energies (ΔG) for these four steps can be calculated as follows in Equations (5-8),

$$\Delta G_1 = \Delta G_{\text{HO}^*} - \Delta G_* + \frac{1}{2} G_{\text{H}_2(\text{g})} - eU \quad (5)$$

$$\Delta G_2 = \Delta G_{\text{O}^*} - \Delta G_{\text{HO}^*} + \frac{1}{2} G_{\text{H}_2(\text{g})} - eU \quad (6)$$

$$\Delta G_3 = \Delta G_{\text{HOO}^*} - \Delta G_{\text{O}^*} + \frac{1}{2} G_{\text{H}_2(\text{g})} - eU \quad (7)$$

$$\Delta G_4 = \Delta G_{\text{O}_2(\text{g})} + \Delta G_* - \Delta G_{\text{HOO}^*} + \frac{1}{2} G_{\text{H}_2(\text{g})} - eU \quad (8)$$

In principle, the OER on a given catalyst might be limited by any of four reaction steps. The most positive value among ΔG_1 , ΔG_2 , ΔG_3 , and ΔG_4 determines the overpotential of OER, and then the catalytic performance can be determined. As shown in **Fig. 2a**, an ideal OER catalyst requires all the four elemental steps with reaction free energies of the same magnitude at *U* = 0 (that is 1.23 eV), but this ideal situation is almost impossible.^{45, 50} This is because the adsorption energies of OER intermediates including HO*, HOO*, and O* species that participate in AEM are linearly correlated.⁴⁵ Especially, because both HOO* and HO* bind with the catalyst surface through oxygen atom via a single bond, the binding energies of HO* and HOO* are tightly linked (**Fig. 2b**) with a constant difference ($\Delta G_{\text{HOO}^*} - \Delta G_{\text{HO}^*}$) of 3.2 ± 0.2 eV for either metals or oxide surfaces regardless of the binding site. From this scaling relation, the following three important implications can be obtained. First, the value of ΔG_{HOO^*} can be directly obtained from the calculated ΔG_{HO^*} , and vice versa, reducing the required computational cost to assess the activity of a given catalyst. Second, since the difference between ΔG_{HO^*} and ΔG_{HOO^*} is greater than the value of 2.46 eV (2×1.23 eV) expected for the ideal catalyst, a minimum theoretical overpotential of 0.37 eV [$(3.2 - 2.46 \text{ eV})/2$] can be concluded. This has been confirmed by the observation from the benchmarked electrocatalysts in the related experimental study.¹⁰ Third, since ΔG_1 or ΔG_4 rarely acts as the potential-determining step in most of OER catalysts, the difference between ΔG_{O^*} and ΔG_{HO^*} ($\Delta G_{\text{O}^*} - \Delta G_{\text{HO}^*}$) can be used as a universal descriptor to predict their OER activity (**Fig. 2c**).¹⁰ The overpotential can be expressed as $\eta^{\text{OER}} = \{\max[(\Delta G_{\text{O}^*} - \Delta G_{\text{HO}^*}), 3.2 \text{ eV} - (\Delta G_{\text{O}^*} - \Delta G_{\text{HO}^*})]/e\} - 1.23$. According to Sabatier principle, an ideal catalyst requires the adsorption strength of the key intermediates to be neither too strong nor too weak. Therefore, the plot of η^{OER} as a function of $(\Delta G_{\text{O}^*} - \Delta G_{\text{HO}^*})$ leads to the universal volcano-shaped relationship independent of the catalytic materials.

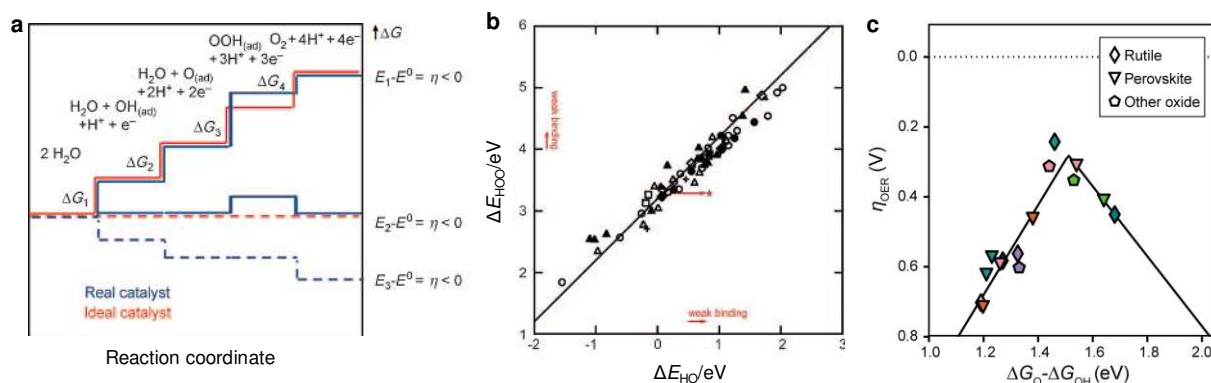


Fig. 2 (a) Gibbs free energies at *U* = 0 for the ideal and real catalysts. Copyright 2010, Wiley-VCH. (b) Adsorption energy of HOO* plotted against the adsorption energy of HO* on perovskite, rutile, anatase, Mn₂O₃, Co₃O₄, and NiO oxides. (a, b) are reproduced from ref. ⁴⁵ with permission from Wiley-VCH Copyright 2011. (c) OER volcano plot for rutile, perovskite and other oxides. Reproduced from ref. ¹⁰ with permission from Macmillan Publishers Limited, Copyright 2016.

2.2 Design efficient OER catalyst based on ($\Delta G_{\text{O}^*} - \Delta G_{\text{HO}^*}$)

The scaling relation provides a guideline for the rational design of efficient catalyst. According to the volcano plot of η^{OER} versus ($\Delta G_{\text{O}^*} - \Delta G_{\text{HO}^*}$), the formation of HOO* species is the potential-determining step for the strong oxygen-binding branch at the left-hand side (**Fig. 2c**).⁴⁵ On the other hand, the deprotonation of HO* species is the potential-determining step for the weak oxygen-binding branch of

volcano plot at the right-hand side. Therefore, the catalyst with oxygen binding neither too strong nor too weak leading to ($\Delta G_{\text{O}^*} - \Delta G_{\text{HO}^*}$) of 1.6 eV shows the optimal activity. It is possible to obtain an excellently active catalyst by regulating the electronic structure to optimize the value of $\Delta G_{\text{O}^*} - \Delta G_{\text{HO}^*}$. The strategies mainly include substituting with foreign elements,⁵¹⁻⁵⁸ generating vacancies,^{25, 59-62} tuning strain,⁶³⁻⁶⁵ and engineering interface.^{43, 66-70}

2.2.1 Substitution of foreign elements. The energetics of OER intermediates can be modulated by the incorporation of other elements into the lattice so that the optimized catalytic activity can be expected. For example, Carter and co-workers performed DFT + U calculations for investigating the effect of cation (by replacing Fe with Ti, Mn, Co, and Ni) and anion (by replacing O with F or Si) substitutions on the water oxidation reaction on the surface of α -Fe₂O₃ (Fig. 3a).⁵⁶ The results show that the reaction energetics at pure or substituted α -Fe₂O₃ surfaces can be described by a volcano plot. At the pure hematite surface, the ($\Delta G_{O^*} - \Delta G_{HO^*}$) is at the right leg of volcano plot, indicating that the oxygen binds too strongly. Substituting Fe by more electronegative elements such as Co or Ni leads to a slightly weaker oxygen binding energy. As such, the generated moderately charged O anions could balance the binding energies among O*, HO*, and HOO*, thereby giving the smallest reaction overpotential. Similarly, binary metal oxides such as CoV,⁵⁷ Co-Fe,⁵⁸ NiV⁵³ and Ni-Fe⁷¹ have also been investigated. Their activity can be also explained by the optimal value of $\Delta G_{O^*} - \Delta G_{HO^*}$. Introduction of the second metal cation into the metal oxides may cause the undesired phase separation,^{72, 73} leading to a limited optimization of ($\Delta G_{O^*} - \Delta G_{HO^*}$) towards the optimal value of 1.6 eV. To further improve the OER activity, some researchers have focused on the formation of ternary metal oxides.^{55, 74-78} For example, Sargent and co-workers reported that the gelled FeCoW oxyhydroxide (G-FeCoW) with atomically homogeneous distribution exhibited a very low overpotential.⁷⁸ X-ray absorption and computational studies reveal that local coordination environments and electronic structures are subtly modulated by the synergistic interplay among W, Fe, and Co, which enables G-FeCoW to give an optimal binding energy of intermediates with the calculated overpotential approaching to 0.4 eV (Fig. 3b). As a result, G-FeCoW shows the higher activity than the annealed one (A-FeCoW), gelled FeCo without W, and even benchmarked NiFeOOH.

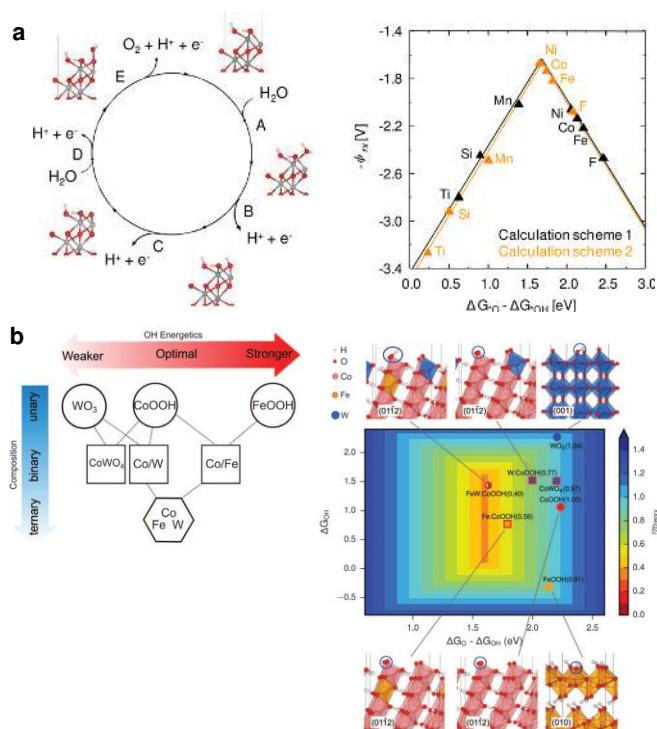


Fig. 3 (a) Tuning the energetics of OER intermediates on hematite via element substitution. Reproduced from ref. 56 with permission from American Chemical Society, Copyright 2012. (b) Tuning the energetics of OER intermediates on CoOOH via alloying with Fe and W. Reproduced from ref. 78 with permission from American Association for the Advancement of Science, Copyright 2016.

2.2.2 Vacancies. Many researchers have reported that the vacancies (including anion and cation vacancies) in the catalyst can tune the surface charge distribution of materials, which gives opportunity to further promote OER.^{25, 59-62, 79, 80} Generating oxygen vacancies has been reported extensively.^{81, 82} Qiao and co-workers reported the regulation of electronic structure of one-dimensional CoO single-crystal by introducing oxygen vacancies, thereby enhancing the charge transfer and optimizing energetics for OER.⁶⁰ In addition, the physical and chemical properties can also be altered by introducing cation vacancies to improve the activity of catalyst.^{59, 83, 84} Wang and co-workers reported the generation of Sn-vacancies by Ar plasma treatment on SnCoFe perovskite hydroxide (SnCo_{0.9}Fe_{0.1}(OH)₆), which decreases the coordination numbers of active sites, thereby promoting the reactant adsorption and charge transfer.⁵⁹ As a result, for SnCoFe perovskite hydroxide with Sn vacancy, an optimal adsorption energy of intermediates leads to a low overpotential of 0.43 eV with the moderate oxygen adsorption strength at Co site. Consistent with the prediction, SnCoFe perovskite hydroxide with Sn vacancy shows significantly enhanced OER activity over the pristine SnCoFe perovskite hydroxide.

2.2.3 Strain. Strain engineering is a useful mean to alter the binding energy of metal-oxygen bond.⁸⁵ Tensile strain is beneficial for filling the in-plane ($d_{x^2-y^2}$) orbitals, while compressive strain is beneficial for filling the out-of-plane (d_{z^2}) orbitals.^{85, 86} Due to the changes in orbital overlap, the binding energy of adsorbed intermediates are optimized.^{63-65, 87} Shao-Horn and co-workers for the first time reported, using LaCoO₃ as a model, the moderate tensile strain can increase OER activity by optimizing the orbital filling.⁶⁵ Recently, Lee and co-workers investigated the OER activity trend of LaNiO₃ by controlling the strain degree from -2.2% to 2.7% using different lattice-mismatched substrates.⁶³ They found that the moderate compressive strain can enhance their activity due to weakened M-O bonding.

2.2.4 Interface. Hybridizing the catalytically active phase with the conducting support materials may not only enhance the charge transfer, but also improve the activity of the active site.⁸⁸ It has been found that the catalyst support (substrate) can change the binding energy of the reaction intermediate through disturbing the electronic structure of the active site or directly participating in the reaction.^{33, 54-58, 76, 77} For example, Jaramillo, Vojvodica and co-workers reported that the use of a Ce⁴⁺ dopant and an Au support could significantly enhance OER activity of electrodeposited NiO_x films (Fig. 4).⁶⁸ Combining experimental observations and theoretical calculations, they demonstrated that all the components of Ni, Ce and Au are crucial in optimizing the adsorption energies of intermediates through the synergistic electronic and geometric effects. The hybrid structure of Ni-based oxide and Au facilitates the access of reactants and intermediates to geometrically under-coordinated Ni ions at the interface between the substrate and the catalyst. The binding energies for key OER intermediates at this interface site are tuned to get close to optimal ones.

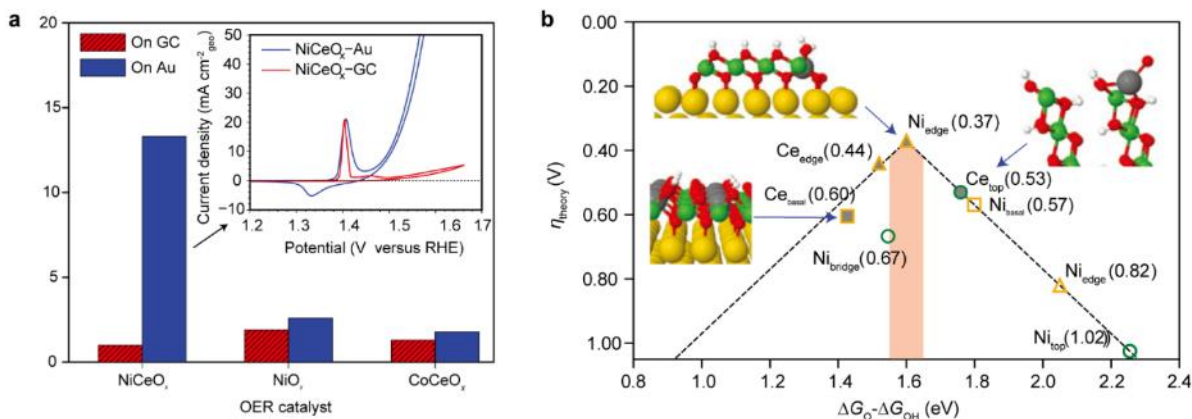


Fig. 4 (a) Experimental and (b) theoretical OER performance of NiCeO_x-Au. Reproduced from ref. 68 with permission from Macmillan Publishers Limited, Copyright 2016.

2.3 Other descriptors

In the past decades, great efforts have been made to identify the surface electronic structure that is proportional to the binding energy of oxygen at metal and oxide surfaces, which can be used as descriptor to readily describe the structure-activity relationship of the catalyst. Through the unremitting efforts, more than 15 descriptors have been found and proposed,⁸⁹ including e_g filling,⁹⁰⁻⁹² OH-M²⁺ bond strength,⁹³ d -band center,^{94, 95} p -band center,⁹⁶ the number of outer electrons,⁹⁷ bulk thermochemistry,⁹⁸ coordinatively unsaturated metal cation (M_{CUS}),⁹⁹ metal-oxygen hybridization,¹⁰⁰ degree of geometric tilting,¹⁰¹ charge transfer energy,¹⁰² magnetic moment,¹⁰³⁻¹⁰⁵ and so on. Here we choose the e_g orbital occupancy and the metal-oxygen covalency, which are two of the most popular descriptors, to exemplify how these descriptors significantly influence the OER activity.

2.3.1 e_g orbital occupancy. The e_g orbital of surface transition metal ions in perovskites participate in σ -bonding with surface adsorbates (Fig. 5a).¹⁰⁶ The binding strength with oxygen-containing intermediates are dependent on the e_g orbital occupancy: the lower e_g occupancy, the stronger binding of oxygen, and vice versa. Starting from this molecular orbital principles, Shao-Horn and co-workers conducted a systematic investigation on the perovskites, and proved that the e_g occupancy of the 3d electron can be used as an activity descriptor for perovskites. The optimal OER activity is obtained when the e_g occupancy is close to unity (Fig. 5b).⁹⁰ Later on, it was found that this descriptor can be also used for explaining the OER on spinel oxides after geometric occupation correction (Fig. 5c, d).⁹¹ In general, the e_g orbital occupation of transition metal 3d electron in octahedral site can be regulated by tuning its oxidation state^{79, 107-111} and spin state.¹¹²⁻¹¹⁵

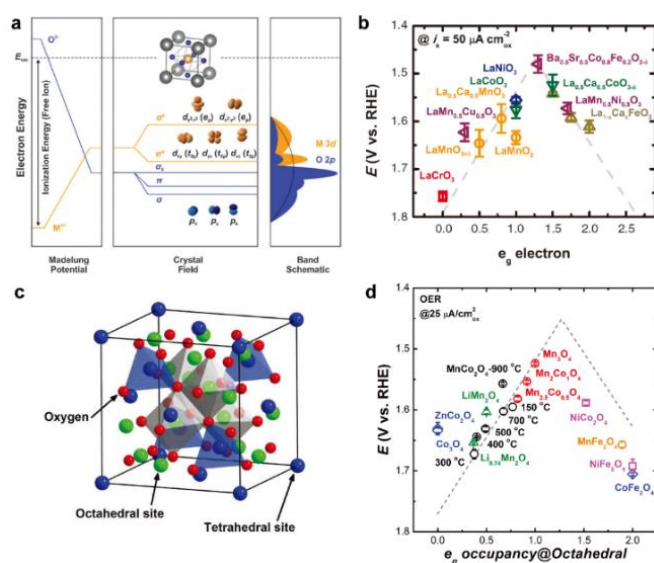


Fig. 5 (a) Schematic band structure for the perovskite oxides (unit cell inset). (a) is reproduced from ref. 106 with permission from Royal Society of Chemistry, Copyright 2015. (b) The relation between OER activity and e_g occupancy of the transition metal cations (B in ABO₃). (b) is reproduced from ref. 90 with permission from American Association for the Advancement of Science, Copyright 2011. (c) Spinel crystal structure. (d) OER activity on various spinel oxides as a function of e_g occupancy of the active element at octahedral site. (c, d) are reproduced from ref. 91 with permission from Wiley-VCH, Copyright 2017.

Oxidation state. The number of d -electron is determined by the oxidation state of the metal cation. Mn³⁺(3d⁴) and Fe⁴⁺(3d⁴) typically gives $t_{2g}^3e_g^1$ configuration with high spin state, while Mn⁴⁺(3d³) and Fe³⁺(3d⁵) gives $t_{2g}^3e_g^0$ and $t_{2g}^3e_g^2$ configuration, respectively in oxides.^{91, 106, 116} Similarly, Ni³⁺(3d⁷) shows the $t_{2g}^6e_g^1$ configuration with low spin state, while Ni²⁺(3d⁸) shows the $t_{2g}^6e_g^2$ configuration. Substitution with cations of different valences and electronegativities or formation of vacancy in oxide lattices can effectively tailor the 3d electron occupancy and the oxidation state of octahedral metal centers. That further optimizes the catalytic properties. The presence of oxygen vacancy in CaMnO₃ could decrease the oxidation state of Mn and increase the occupancy of e_g . Based on this, Yang and co-workers reported the synthesis of oxygen-deficient perovskite CaMnO_{2.5} through the reductive treatment of CaMnO₃.⁷⁹ The removal of lattice oxygen from CaMnO₃ changed the electron configuration of Mn⁴⁺(3d³) to high spin state Mn³⁺(3d⁴) in CaMnO_{2.5}. This high spin state orbital with e_g electron of 1 in Mn ion would lead to a moderated adsorption strength for oxygen-related intermediate species. As a result, the oxygen-deficient CaMnO_{2.5}

shows a better OER activity than the pristine CaMnO_3 .

Spin state. It should be noticed that the e_g occupancy of the active metal site is determined by both its oxidation state and spin state (Fig. 6a).¹⁰⁶ For example, the low spin state Co^{3+} shows an electron configuration of $(\text{LS } t_{2g}^6 e_g^0)$. Changing its electron configuration to an intermediate spin state $(\text{IS } t_{2g}^5 e_g^1)$ has been expected to significantly improve the OER activity. Strain engineering,^{65, 115} nanostructuring,^{112, 113, 117} and doping^{114, 118} have been found effective in tuning the spin state. For example, Wu and co-workers demonstrated a spin-state regulation method to optimize OER activity by controlling the lattice orientation of LaCoO_3 films (Fig. 6b).¹¹⁵ The varied orientations generate different degrees of distortion of the CoO_6 octahedron, switching the spin-state of cobalt into intermediate spin-state. As a result, $\text{LaCoO}_3(100)$ film exhibits better OER performance than the other two films with (110) and (111) orientations due to the optimal e_g electron filling. Zeng and co-workers successfully tuned the e_g filling of Co ions close to the optimal configuration of 1.2 by decreasing the particle size of LaCoO_3 to induce spin-state transition from low-spin state to high-spin state for cobalt cations at the surface.¹¹⁷ The dimensional confinement can also modify the electronic structure of the catalyst. Wei and co-workers fabricated an atomically thin $\gamma\text{-CoOOH}$ nanosheet by an “atomic-scale phase transformation” strategy (Fig. 6c).¹¹² Co 2p XPS and EXAFS results confirmed that the dimensional confinement generated a large number of dangling bonds on the surface Co octahedron (CoO_{6-x}) with a structural distortion. In addition, the orbital degeneracy is broken with the rearrangement of the Co 3d electron population, leading to the partially occupied e_g orbitals and partially unoccupied t_{2g} orbitals. Consequently, the ultrathin $\gamma\text{-CoOOH}$ nanosheet possess superior catalytic water oxidation activity. Recently, Fe substitution has been reported as an efficient method to transform Co^{3+} spin state from generally low spin state to intermediate spin state $(\text{IS } t_{2g}^5 e_g^1)$, which leads to an enhanced intrinsic OER activity of LaCoO_3 as well.¹¹⁴

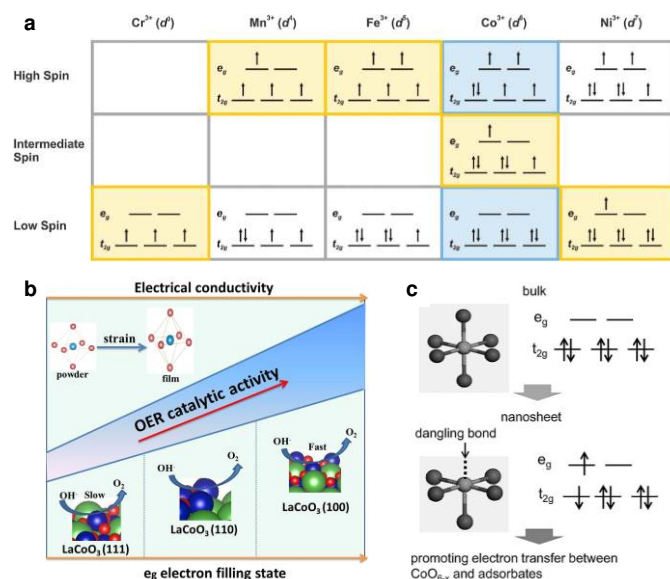


Fig. 6 (a) The e_g orbital occupancy of some transition metal cations with different spin states. Reproduced from ref. 106 with permission from Royal Society of Chemistry, Copyright 2015. (b) Spin-state regulation by lattice-oriented control of LaCoO_3 epitaxial strain. Reproduced from ref. 115 with permission from Elsevier, Copyright 2017. (c) Orbital filling transformation of ultrathin $\gamma\text{-CoOOH}$ nanosheet to promote water oxidation. Reproduced from ref. 112 with permission from Wiley-VCH, Copyright 2015.

2.3.2 Metal-oxygen covalency. Although e_g orbital occupancy is a

powerful activity descriptor, it cannot explain why LaMnO_3 , LaCoO_3 and LaNiO_3 with the same e_g orbital occupancy ($e_g = 1$) have different OER activities. This weakness is because the e_g orbital occupancy of metal cation is established on the ionic model and does not capture the sharing of electrons along metal-oxygen bond.¹¹⁶ Actually, both metal and oxygen can function as active sites for highly covalent late-transition-metal oxides. To capture the mixed ionic-covalent feature of the metal-oxygen bond, the descriptor using the metal-oxygen covalency has been established. Shao-Horn and co-workers proposed that the enhanced OER activity can be obtained by improving the covalent mixing (the parameter is defined as $\text{hole}_{e_g} + 1/4\text{hole}_{t_{2g}}$ by the normalized soft X-ray absorbance) between the octahedrally coordinated metal cation (B site in perovskite oxides) and O anions at the constant e_g filling of 1 (Fig. 7a).⁹⁰ Greater metal-oxygen covalency indicated that the active redox couple of the B-site cation has a larger O-2p character, enhancing the charge transfer between active sites and adsorbates in the rate-determining steps of OER. Later, they used O p -band center to quantify the metal 3d-O 2p orbital hybridization (Fig. 7b).⁹⁶ Moving the computed O p -band center closer to the Fermi level can increase OER activities, but the stability of oxides would decrease when the O p -band center is too close to the Fermi level. In Fig. 7c, they further illustrated the essence of the covalency of metal-oxygen bond, which is quantified by charge-transfer energy (energy difference between unoccupied metal 3d- and occupied O 2p-band centers). The covalency linearly scales with the oxygen vacancy formation energy, oxygen binding energy, and electron transfer barrier associated with OER.¹¹⁶ Therefore, the covalency can determine the overall OER activity of a catalyst. More examples have been given by Yagi and co-workers. They used the covalency to explain why the activity $\text{CaCu}_3\text{Fe}_4\text{O}_{12}$ is higher than LaMnO_3 with the similar e_g orbital occupancy of unit.^{119, 120} Compared with Mn^{3+} , the 3d-orbital energy levels of Fe^{4+} ion are lower than that of the O 2p orbitals, indicating the enhanced metal-oxygen covalency. Moreover, compared with SrFeO_3 , the large overlapping between Cu (Fe) e_g and O 2p orbitals in square-planar (octahedral) coordination enhances the structural stability of $\text{CaCu}_3\text{Fe}_4\text{O}_{12}$. According to inductive effect, metal substitution can result in the redistribution of electronic density between metal and oxygen in transition metal oxides: metal substituents with higher electronegativity than the parent metal could reduce the energy of the d band, leading to the enlarged metal-oxygen covalency.^{121, 122} The incorporation of other low-valent metals or metal vacancy also increases the oxidation state of the metal, thus lowering the energy of the d band and enlarging metal-oxygen covalency. Our group recently reported that enlarging Co-O covalency can promote OER on spinel oxides by the incorporation of cationic vacancy (Fig. 7d, e).¹²³ The formation energy of Zn vacancy of Fe substituted ZnCo_2O_4 is lower than ZnCo_2O_4 , suggesting Fe can promote the formation of Zn vacancy in the spinel lattice. With the combination of theory and experimental approaches, we found that the Co 3d and O 2p covalency can be enlarged by 10-30 at% Fe substitution. Later, we further used the concept of covalency to explain the octahedral geometry in spinel oxides was more catalytically critical than tetrahedral one.¹²⁴ Co_{Oct} possesses a stronger hybridization with oxygen than that of Co_{Td} , which is confirmed by the analysis of both density of state and Bader charge. As a result, more oxygen charge is polarized into the octahedral metal ion instead of tetrahedral one. Therefore, the specific activity follows the trend of $\text{CoAl}_2\text{O}_4 < \text{ZnCo}_2\text{O}_4 < \text{Co}_3\text{O}_4$. The OER performance of spinel CoAl_2O_4 can be further improved by pushing more active Co into octahedral site (the formation of inverse spinel at the low calcination temperature). On the other hand, the OER performance can be further improved by

partially replacing tetrahedral Zn with Li to facilitate the shift of oxygen charges to the active octahedral TM center, finding an active spinel catalyst $\text{Li}_{0.5}\text{Zn}_{0.5}\text{Fe}_{0.125}\text{Co}_{1.875}\text{O}_4$ (**Fig. 7f, g**).

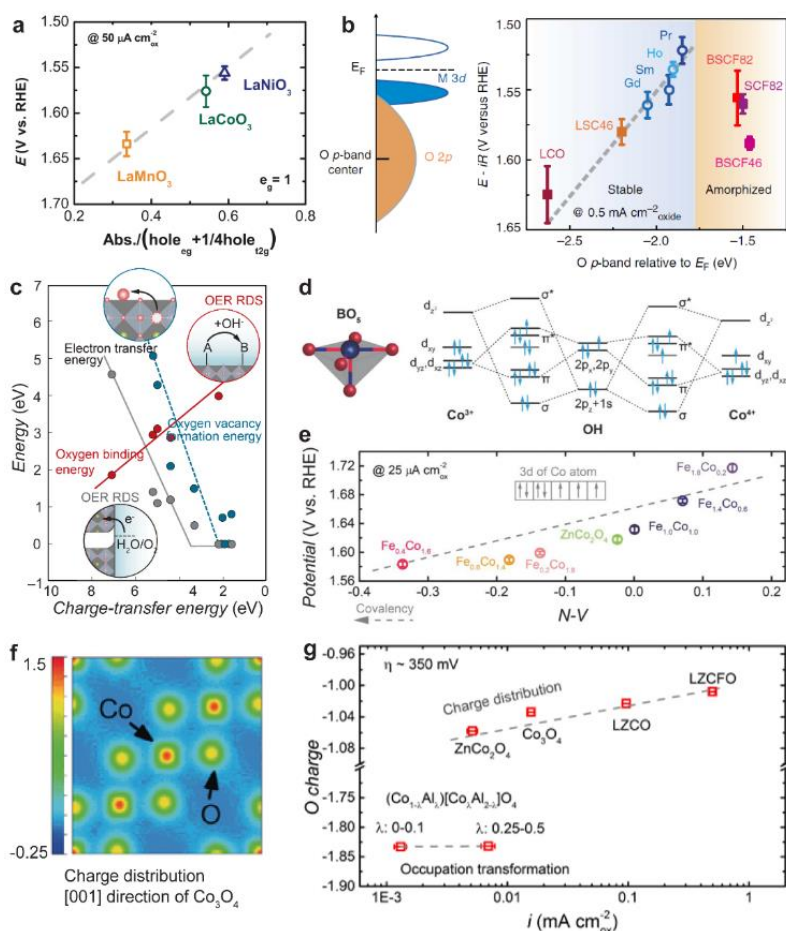


Fig. 7 (a) The role of the metal-oxygen covalency on the OER activity of perovskite oxides (covalency is estimated by the normalized soft X-ray absorbance at e_g filling = 1.). Reproduced from ref. 90 with permission from American Association for the Advancement of Science, Copyright 2011. (b) Computed oxygen p-band centre for oxygen evolution. Reproduced from ref. 96 with permission from Macmillan Publishers Limited, Copyright 2013. (c) Relationship of charge-transfer energy to oxygen vacancy formation (blue), oxygen binding energy (red) and electron transfer energy (gray). Reproduced from ref. 116 with permission from American Association for the Advancement of Science, Copyright 2017. (d) Molecular orbital diagrams for the Co-OH (Co^{3+} , Co^{4+}) bonding at the surface of spinel oxides. (e) The OER activity (potentials at a specific current density of $25 \mu\text{A cm}^{-2}_{ox}$) as a function of the $N-V$ parameter. (d, e) are reproduced from ref. 123 with permission from Wiley-VCH, Copyright 2018. (f) Charge density on of Co_3O_4 on [001] direction. (g) OER activity (specific current density at an overpotential of ~ 350 mV) as a function of computed oxygen charges. (f, g) are reproduced from ref. 124 with permission from Wiley-VCH, Copyright 2019.

3. Design efficient OER catalyst beyond the top of the volcano in AEM

The scaling relation among the OER intermediates, i.e. HO^* , HOO^* , and O^* species, in AEM indicates a cap of the OER activity, where the theoretical overpotential may not be beyond 0.37 eV.^{125, 126} To date, three strategies have been emerged to break this scaling relation for better activity. The first one is to stabilize the OER intermediate HOO^* without affecting the adsorption of HO^* . The second is to introduce proton acceptor to modify the reaction pathway. Third is to activate lattice oxygen for a direct O-O radical coupling, which in most cases is called lattice oxygen-mediated mechanism (LOM). LOM could bypass the generation of immediate HOO^* . Thus, the limitation caused by the adsorption-energy scaling relation between HO^* and HOO^* can be avoided.

3.1 Stabilizing of HOO^* independent on HO^*

If the HOO^* and HO^* have the capacity for distinct interactions with the catalyst, breaking the cap of OER activity in scaling relation and reducing OER overpotential close to 0 V may be possible. Considerable efforts have been devoted to finding a way to alter the

adsorption of HOO^* and HO^* independently. To date, dual-site mechanism¹²⁷ and formation of hydrogen bond¹²⁸ are two of the most effective methods to stabilize HOO^* .

3.1.1 Dual-site mechanism. AEM is proceeded through HO^* , O^* , HOO^* and O_2^* . Controlling the adsorption of HO^* and HOO^* on two different sites would break the related scaling relation. For example, Huang and co-workers reported the synthesis of single-atom transition metals (Fe, Co and Ni) embedded in N-doped graphene (M-NHGFs) by thermal annealing method.¹²⁷ Though M-NHGFs has an identical MN_4C_4 moiety, their catalytic properties are different due to the tuned ligand-field effect by different metal centers. In MN_4C_4 moieties, both M and C are the possible adsorption sites for the intermediates. Whether the dual sites involve in the adsorption of OER intermediates depends largely on the number of d electrons (N_d) of the metal. Different from Co and Fe that follow AEM mechanism at single metal site, OER proceed through a dual-site mechanism on NiN_4C_4 moieties (**Fig. 8a-c**). In detail, OER intermediates including O^* and HO^* are adsorbed on the C site, while the HOO^* is adsorbed on

the Ni site, leading to the adsorption energy difference between HOO^* and HO^* no longer 3.2 eV. As a result, the Ni-NHGF following the dual-site mechanism shows higher catalytic activity than Co-NHGF and Fe-NHGF.

3.1.2 Formation of hydrogen bond. The structure of HOO^* is more sensitive than that of HO^* , because the pendent O in HOO^* may produce an additional interaction with different catalyst structure compared to HO^* . Therefore, the HOO^* adsorbate can be more easily stabilized than HO^* , and the scaling relation between them can be broken. Vojvodic and co-workers proposed a strategy to break the scaling relations by defining a three-dimensional nanoscopic catalyst structure, which provides a confined reaction environment to enable

selective interaction with the specific intermediate.¹²⁸ The scheme is, the nanoscopic catalyst structure enables selective interaction with HOO^* intermediate (the adsorption of HO^* unaffected). Using RuO_2 and IrO_2 (110) surfaces as models, they introduced the second surface to form a channel (**Fig. 8d**). The relationship between HO^*/HOO^* adsorption with the channel width were investigated. The results show that the binding energies of HO^* are constant for the channel $> 6 \text{ \AA}$. In contrast, the binding energy of HOO^* shows the lowest value at about 6 \AA (**Fig. 8e**), indicating that there is a stabilizing interaction between HOO^* and the O atom in opposite channel surface through the formation of specific hydrogen bond. As a result, the overpotential for RuO_2 decreases to roughly 0.2 eV for the channel about 7 \AA , which is lower than the optimal theoretical overpotential (about 0.4 eV) predicted by the scaling relation.

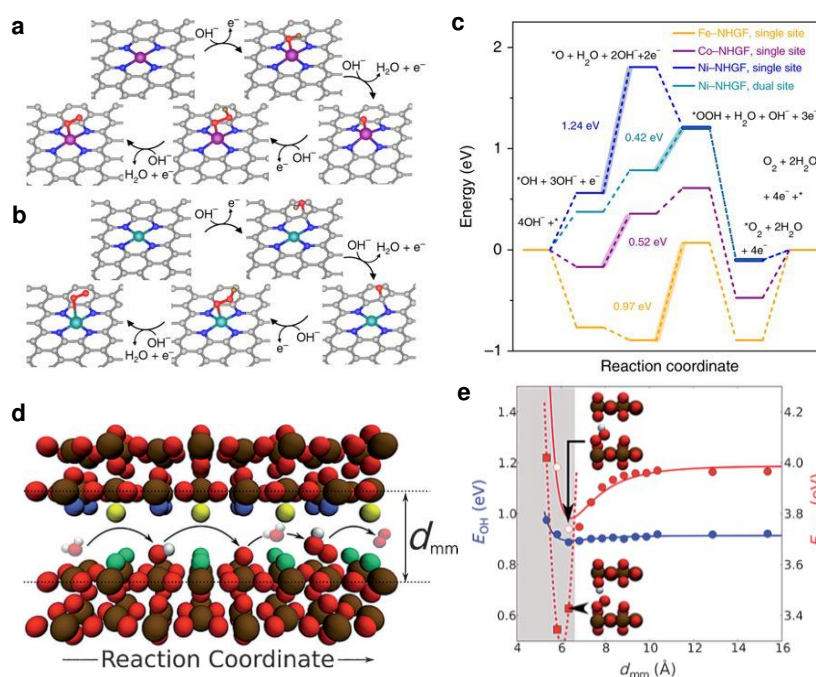


Fig. 8 Proposed reaction scheme with the intermediates having optimized geometry of (a) the single-site and (b) dual-site mechanisms towards OER. (c) Free energy diagram for OER over Fe-NHGF, Co-NHGF and Ni-NHGF with a single-site mechanism, and Ni-NHGF with a dual-site mechanism at 1.23 V vs RHE. (a-c) are reproduced from ref. 127 with permission from Macmillan Publishers Limited, Copyright 2018. (d) Atomistic side-view of the model system used to simulate confinement, where the reaction is assumed to take place as the channel width (d_{mm}) decreases. (e) Adsorption energies of HO^* and HOO^* as a function of channel width. (d, e) are reproduced from ref. 128 with permission from Wiley-VCH, Copyright 2015.

3.2 Introduction of proton acceptor

The formation of hydrogen bonds is beneficial to the stability of HOO^* , but this stabilizing effect on HOO^* is very limited. Introducing a proton acceptor is one of the most effective methods for stabilizing the HOO^* intermediate to produce the OO^* and H^* ($\text{OO}^* + \text{H}^*$). Proton acceptor is a fully independent site, which can further stabilize the intermediate ($\text{OO}^* + \text{H}^*$), resulting in a great improvement of catalytic activity.¹²⁹⁻¹³¹ The catalytic cycle is proceeded by the single metal and the combined proton acceptor sites. Up to now, two methods to introduce a proton acceptor have been reported. One method is to substitute elements with higher electronegativity, which can activate oxygen on the surface as a proton acceptor. The other is to functionalize the catalyst surface with strong nucleophilic groups for accepting hydrogen, such as phosphate (Pi). The details of these two methods are introduced below.

3.2.1 Substitution by metals with higher electronegativity.

The scaling relation of adsorption energies among reaction intermediates can be broken by modifying the active site. Rossmeisl and co-workers proposed that the oxygen atoms on bridge positions of RuO_2 surface can be activated as a proton acceptor by substituting Ru with Ni or Co.¹³² On Ni and Co substituted surface, the H atom in HO^* and HOO^* will be transferred to the neighboring activated oxygen, forming $\text{O}^* + \text{H}^*$ and $\text{OO}^* + \text{H}^*$, respectively. Different from the traditional scaling relation of HOO^* and HO^* , the adsorption energy difference between $\text{OO}^* + \text{H}^*$ and $\text{O}^* + \text{H}^*$ is decreased below 3.2 eV. As a result, the largest free energy step amounts to 1.49 eV and 1.33 eV for the Ni and Co substituted RuO_2 , respectively. The resulted overpotentials (0.26 and 0.10 eV) are significantly lower than the highest value of volcano (0.37 eV). Later, Shao-Horn and co-workers used *in situ* surface X-ray scattering measurements combined with density functional theory (DFT) to determine the potential-dependent surface structure on single-crystal $\text{RuO}_2(110)$ in acidic electrolyte.¹²⁹ At OER potential window, the OO^* species was detected on the undercoordinated Ru sites, which was stabilized by a neighboring HO^* group on the undercoordinated Ru site or bridge site. In this reaction pathway, the subsequent deprotonation of HO^*

was found to be potential-determining. Recently, the similar observation has been also reported on Co_3O_4 , CaMnO_3 and NiFeO_x surfaces (Fig. 9a).^{131, 133, 134} For example, Hu and co-workers demonstrated that for $\gamma\text{-NiOOH}$ with nanoclusters of $\gamma\text{-FeOOH}$, Fe can function as the oxygen evolving center (*OO) and a nearby terrace O site on the $\gamma\text{-NiOOH}$ can act as a proton acceptor (*H).¹³⁴

3.2.2 Introduction of nucleophilic group. Phosphate ion groups (Pi) have a strong nucleophilic property and well-adapted pKa of 12.67, therefore it is suitable as a proton acceptor to functionalize the catalyst surface. Grimaud and co-workers reported that Pi functionalization can significantly enhance the interfacial proton transfer on perovskite surfaces (Fig. 9b).¹³⁵ As a result, $\text{La}_{0.5}\text{Sr}_{0.5}\text{CoO}_{3-\delta}$

δ functionalized by Pi shows the significantly enhanced OER activity, which is about two times higher than that of the unmodified $\text{La}_{0.5}\text{Sr}_{0.5}\text{CoO}_{3-\delta}$ and one order of magnitude higher than that of LaCoO_3 . Similarly, Shao and co-workers constructed a hybrid catalyst with $\text{Sr}_3\text{B}_2\text{O}_6$ as a proton acceptor to functionalize A-site deficient $\text{Sr}_{0.8}\text{Co}_{0.8}\text{Fe}_{0.2}\text{O}_{3-\delta}$ perovskite.¹³⁶ With the improved interfacial proton transfer, the as-synthesized $\text{Sr}(\text{Co}_{0.8}\text{Fe}_{0.2})_{0.7}\text{B}_{0.3}\text{O}_{3-\delta}$ hybrid catalyst shows a 2.7-fold higher OER activity than the unmodified one at the overpotential of 350 mV. Additionally, they demonstrated that using $\text{Sr}_3\text{B}_2\text{O}_6$ as a proton acceptor can be expanded for other high covalent oxides including $\text{La}_{0.4}\text{Sr}_{0.6}\text{CoO}_{3-\delta}$, $(\text{Pr}_{0.5}\text{Ba}_{0.5})\text{CoO}_{3-\delta}$ and $\text{Ba}_{0.5}\text{Sr}_{0.5}\text{Co}_{0.8}\text{Fe}_{0.2}\text{O}_{3-\delta}$.

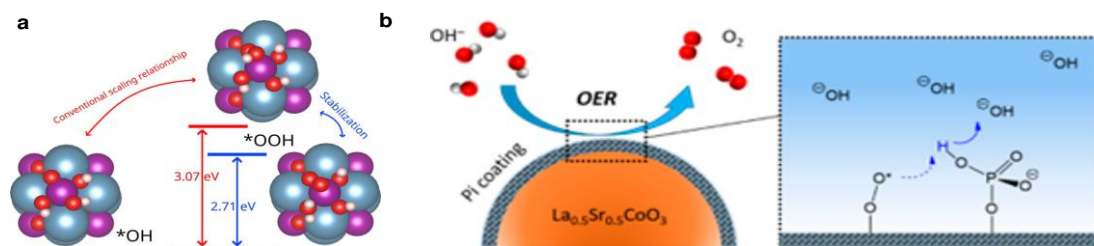


Fig. 9 (a) Breaking the conventional scaling relation on CaMnO_3 by activating surface oxygen as a proton acceptor. Reproduced from ref. 131 with permission from American Chemical Society, Copyright 2018. (b) Phosphate ion functionalization of perovskite surfaces as a proton acceptor to promote OER. Reproduced from ref. 135 with permission from American Chemical Society, Copyright 2017.

3.3 Lattice oxygen-mediated mechanism (LOM)

LOM proceeds on two neighboring metal sites, which is different from the conventional AEM on single metal site (Fig. 10a, b).¹²¹ Firstly, two HO^* on metal sites go through the deprotonation, resulting in two metal-oxo species. Secondly, these two neighbouring oxo species directly couple to form O-O bond instead of combining with water or OH^- to form HOO^* . Finally, O_2 is released with the bareness of two vacant metal centers that are subsequently occupied by OH^- . Because HOO^* is not an intermediate in the LOM catalytic cycle,

water oxidation following LOM is free from the limitation (minimal overpotential about 0.37 V) of scaling relation between HO^* and HOO^* . In the past decades, LOM by direct O-O coupling to form O_2 is not concerned with heterogeneous water oxidation catalyst, because this process is considered to need a large activation barrier. In fact, this process has been widely accepted to operate in certain molecular catalysts involving transition metals.¹³⁷⁻¹⁴⁰ In this part, we introduce the significant progress of LOM for OER in recent years and the catalyst design methods.

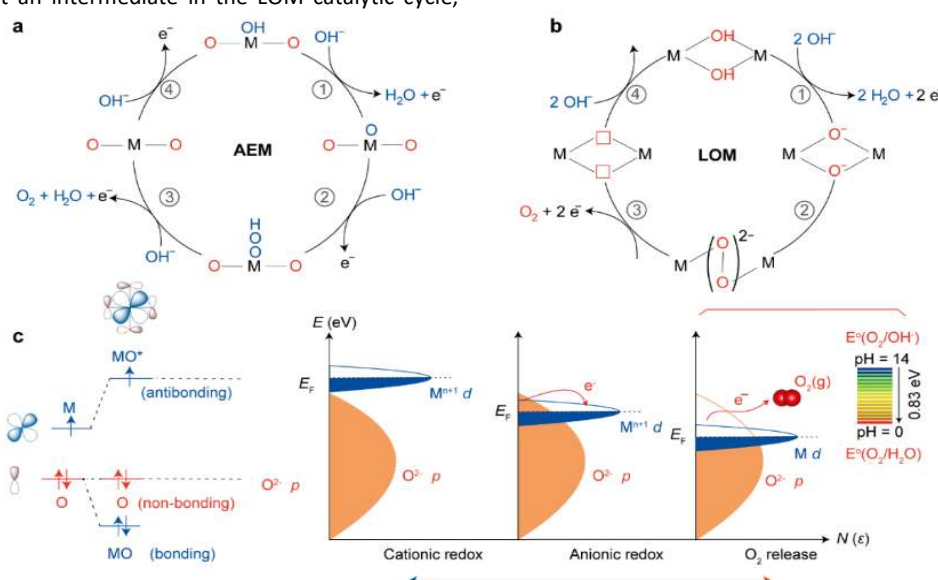


Fig. 10 (a, b) Schematic illustration of OER mechanisms, including AEM and LOM, respectively. (c) Schematic band structure of perovskite oxides to demonstrate the different redox processes as the energy of $M d$ band decreases with respect to the $\text{O } 2p$ band. Reproduced from ref. 121 with permission from Macmillan Publishers Limited, Copyright 2016.

3.3.1 LOM in perovskite. The general formula of perovskites is ABO_3 , where B site represents the smaller transition metal ions in corner-shared BO_6 octahedra and A site represents the larger cations through 12-fold coordination with O. The nature of the metal-oxygen bond in the perovskite structure, that is metal-oxygen covalency, provides a basis for tailoring the electronic structure to control OER mechanism of LOM (Fig. 10c).^{116, 121} When metal d band is located above the oxygen p band, the metal center of oxides acts as the adsorption site and redox center, allowing water oxidation to follow AEM. More specifically, for the OER at 1.23 V vs. RHE, the redox center needs to donate or receive electrons whose energy is close to the thermodynamic potential of oxygen in water. When the energy of the occupied metal d band is lower than that of the oxygen p band, the electrons from p band are transferred to the d band, generating ligand holes. This promotes the formation of oxygenated $(O_2)^{n-}$ species by structural arrangement to reduce its energy getting to stable state. Therefore, the OER mechanism can be switched from AEM to LOM when the metal-oxygen covalency is increased.

Tuning metal-oxygen covalency. As aforementioned, tuning the metal-oxygen covalency is the key for LOM on perovskite oxides.^{102, 116} In 2016, Stevenson and Kolpak and co-workers firstly proposed the LOM in OER and demonstrated the relationship between oxygen vacancies, metal-oxygen covalency, and OER activity (Fig. 11a-c) combining experimental and DFT calculations.^{141, 142} The concentration of oxygen vacancies and Co-O covalency can be well controlled through the incorporation of Sr^{2+} into $La_{1-x}Sr_xCoO_{3-\delta}$ ($0 \leq x \leq 1$). When x is equal to and greater than 0.4, the OER mechanism is

switched from the AEM to LOM with the formation of superoxide-like $-OO(V_O)$ adsorbates (I_1) through coupling of lattice oxygen and adsorption oxygen. Benefiting from the greater Co-O covalency, higher vacancy concentrations and faster oxygen ion diffusion rate, $SrCoO_3$ exhibits the highest specific activity among $La_{1-x}Sr_xCoO_{3-\delta}$ with the involvement of lattice oxygen. Using *in situ* ^{18}O isotope labeling mass spectrometry, Shao-Horn and co-workers further provided the direct experimental evidence of lattice oxygen participation during the OER on Sr^{2+} substituted $La_{1-x}Sr_xCoO_{3-\delta}$ and $SrCoO_{3-\delta}$ (Fig. 11d).¹⁴³ The discovery of LOM challenges the traditional view that electrocatalysis is a surface reaction. They considered that bulk metal-oxygen covalency, governs both the OER activity and related reaction mechanism on transition metal oxides. For highly covalent oxides, the OER can be triggered on the oxygen sites when the electronic states near the Fermi level have evident O 2p character (Fig. 11e). Moreover, they also found that the oxides exhibit pH-dependent OER activity on the scale of reversible hydrogen electrode (RHE) when lattice oxygen oxidation is activated, indicating the presence of nonconcerted proton-electron transfers in the OER mechanism. Two possible nonconcerted reaction pathways are shown in Fig. 11f. It is worth noting that this view, in turn, may not be true. Chorkendorff and co-workers found that the participation of lattice oxygen in $NiFeO_xH_y$ is absent using isotopic labeling, but its catalytic activity is pH-dependent on the RHE scale.^{144, 145} This pH dependence may originate from the deprotonation of surface oxygen groups that affect the kinetics.¹⁴⁶ Our group also demonstrated that $ZnFe_{0.4}Co_{1.6}O_4$ catalyzes OER with AEM, showing pH-dependent activity on the RHE scale.¹²³ More detailed understanding about pH dependence of OER activity on oxides can be referred from Shao-Horn's work.¹⁴⁷

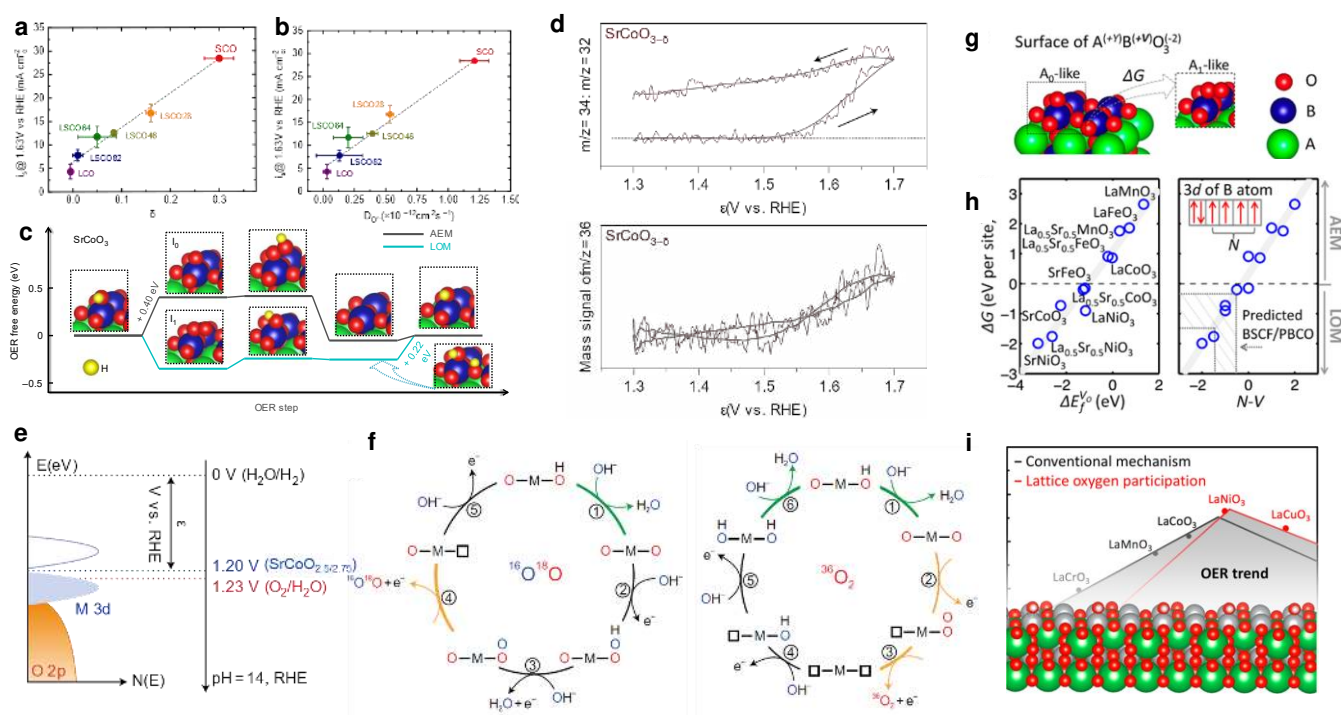
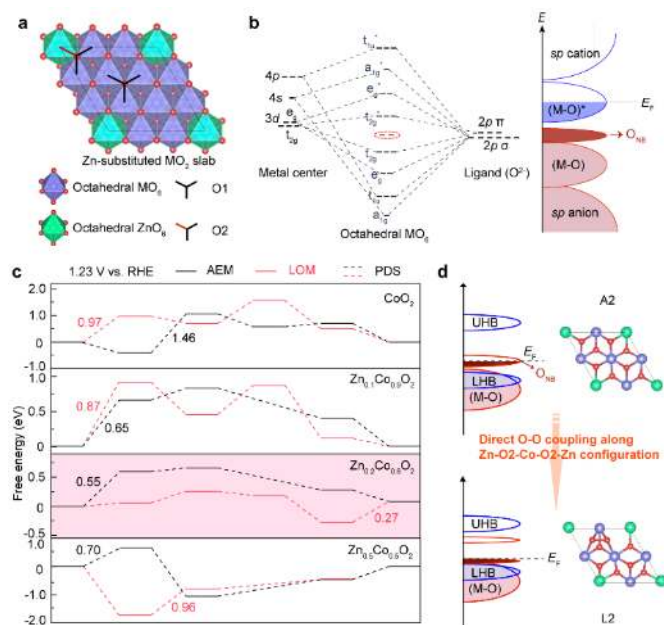


Fig. 11 (a, b) The activity correlations with the vacancy parameter and the oxygen ion diffusion rate on $La_{1-x}Sr_xCoO_{3-\delta}$. (c) The free energy of LOM and AEM on $SrCoO_3$ with indicated intermediates structures and potential-determining steps. (a-c) are reproduced from ref. 141 with permission from Macmillan Publishers Limited, Copyright 2016. (d) Direct evidence of lattice oxygen participated oxygen evolution using ^{18}O -labelled perovskites. (e) Schematic band structure of electrochemical oxygen intercalation into brownmillerite $SrCoO_{3-\delta}$. (d-f) are reproduced from ref. 143 with permission from Macmillan Publishers Limited, Copyright 2017. (g) A0- and A1-like surface structures for AEM and LOM, respectively. (h) Free energy difference between A1- and A0-like intermediates versus bulk V_O formation energy and $N-V$ parameter, where N is the number of unpaired electrons on the isolated B atoms, and V is the nominal charge of B in the stoichiometric bulk ABO_3 . (g, h) are reproduced from ref. 142 with permission from American Chemical Society, Copyright 2016. (i) OER volcano plot on some perovskites with AEM and LOM. Reproduced from ref. 149 with permission from American Chemical Society, Copyright 2018.

Using DFT calculations, Kolpak and co-workers further determined the surface structure under realistic conditions and the OER mechanism on LaNiO_3 and other perovskites (Fig. 11g, h).^{142, 148} They found that the reversible formation of surface oxygen vacancies (V_O) plays the crucial role in LOM. In detail, the participation of surface lattice oxygen (O_surf) is via the nonelectrochemical pathway where the adsorbed oxygen (O^*) diffuses from the metal site to oxygen site, and then O_surf moves out of the surface and reacts with O^* to form $\text{O}_\text{surf}-\text{O}^*$ and one V_O .¹⁴⁸ Moreover, $N-V$ as an effective parameter is proposed to correlate with the OER mechanism, where N is the unpaired electron number of the B atoms, and V is the nominal charge of B in the stoichiometric ABO_3 . Additionally, they demonstrated that LOM can bypass the overpotential limitation imposed by the scaling relation in the conventional AEM (Fig. 11i), which opens a new avenue for the design of better OER catalysts.¹⁴⁹ Stevenson and co-workers recently proposed a Ruddlesden-Popper (RP)-phase oxide of $\text{La}_{0.5}\text{Sr}_{1.5}\text{Ni}_{1-x}\text{Fe}_x\text{O}_{4\pm\delta}$ (LSNF, $0 \leq x \leq 1$) for OER with the activation of lattice oxygen. Sr substitution further oxidizes Ni through charge compensation, enhances Ni-O covalency and electronic conductivity, thereby promoting the high catalytic activity.¹⁵⁰ Introducing chemical substitution of Fe for Ni regulates the overlapping degree between the metal d band and the $\text{O } p$ band. By increasing Fe substitution amount, the average oxidation state of Ni further increases from +3.54 in $\text{La}_{0.5}\text{Sr}_{1.5}\text{NiO}_{4\pm\delta}$ to +3.95 in $\text{La}_{0.5}\text{Sr}_{1.5}\text{Ni}_{1-x}\text{Fe}_x\text{O}_{4\pm\delta}$ ($x = 0.85$), as does the oxygen hyperstoichiometry (δ from 0.013 to 0.036). DFT calculations found the cross-gap hybridization between $e_\text{g}(\text{Ni})$, $p(\text{O})$ and $e_\text{g}(\text{Fe})$ bands around the Fermi level, which improves the charge transfer along Fe-O-Ni bridge and the bandwidth available for catalyst-adsorbate electron transfer. As such, the optimized catalyst of $\text{La}_{0.5}\text{Sr}_{1.5}\text{Ni}_{0.7}\text{Fe}_{0.3}\text{O}_{4\pm\delta}$ exhibited remarkable catalytic activity, with specific activity of $32.7 \text{ mA cm}^{-2}_\text{ox}$ and mass activity of $1930 \text{ mA mg}^{-1}_\text{ox}$ at 1.63 V (vs. RHE), being over 3.5 and 5.0 times more active than the previously reported $\text{SrCoO}_{2.7}$ ($9.2 \text{ mA cm}^{-2}_\text{ox}$, $332 \text{ mA mg}^{-1}_\text{ox}$).

3.3.2 LOM in other materials. In addition to highly covalent perovskites, mass spectrometry has confirmed that other materials such as RuO_2 ,¹⁵¹ IrO_2 ,^{152, 153} Co_3O_4 ,^{154, 155} NiCo_2O_4 ,¹⁵⁶ Co-Pi ,^{157, 158} Ni and NiCo layered double hydroxides (LDHs),¹⁵⁹ Au and so on,¹⁶⁰ evolved O_2 that can come not only from water but also from the oxide lattice. For example, Wohlfahrt-Mehrens and co-workers performed the experiments on an amorphous RuO_2 electrode in acid solution using ^{18}O isotope labeling and differential electrochemical mass spectrometry (DEMS).¹⁵¹ They demonstrated qualitatively that the lattice oxygen exchange reaction occurred during OER. However, no such reaction with the exchange of lattice oxygen occurred on Pt in both acidic and alkaline media.¹⁶¹ Twenty years later, Comninellis and co-workers repeated the measurement and further demonstrated that one layer of IrO_2 unit cells takes part in oxygen evolution.¹⁵² Krtil and co-workers found the oxygen exchange reaction is dependent on the applied potential.¹⁵³ Furthermore, they also reported that the local structure of the catalyst plays an important role in the amount of the lattice oxygen involved in the oxygen evolution because the reactivity of lattice oxygen in $\text{Ru}_{0.9}\text{Ni}_{0.1}\text{O}_{2-\delta}$ is higher than that in RuO_2 . Contrarily, Shao-Horn and co-workers examined whether the participation of lattice oxygen occurs on RuO_2 film with different orientations, and suggested that no lattice oxygen exchange reaction occurs during OER on crystalline RuO_2 surfaces.¹⁶² The discrepancy indicates that the lattice oxygen exchange seems to be dependent on the structure and crystallinity, besides being sensitive to the composition of the material.

For catalysts with non-noble metals, Baltruschat and co-workers used DEMS to study Co_3O_4 and found that the oxide layer participates in OER through the oxygen exchange reaction.¹⁵⁴ The number of lattice oxygen participating in OER accounts for 0.1-0.2% of the total oxide loading, equivalent to about 10-30% of the surface atoms. Recently, Hu and co-workers combined ^{18}O -labeling experiments with *in situ* Raman spectroscopy to identify the role of lattice oxygen and the negatively charged oxygen species of NiOO^- , in the Fe-free and Fe-containing Ni-based layered double hydroxide (LDH) catalysts.¹⁵⁹ They found that lattice oxygen is participated in the OER for Fe-free Ni-based LDHs, but not for Fe-containing ones. Moreover, NiOO^- is detected as the OER intermediate for Fe-free Ni-based LDHs, but not for Fe-containing ones. We further used DFT calculations to demonstrate that LOM can be triggered in oxyhydroxide, MOOH (M = metal cation).¹⁶³ Different from perovskites, all three $\text{O}(2p)$ orbitals typically involve in M-O bonding in MOOH without the presence of oxygen non-bonding (O_NB) states.^{164, 165} O_NB is the prerequisite to generate peroxo- or superoxo-like O-O intermediate without the risk of structural instability.¹⁶⁴⁻¹⁶⁶ Using CoOOH as a model material, the incorporation of low-valence and catalytically inactive $\text{Zn}^{2+}(d^{10})$ ions can form accessible O_NB states and increase Co-O covalency simultaneously (Fig. 12a, b).¹⁶³ Combining theoretical and experimental approaches, creating oxygen holes in O_NB states along the specific Zn-O2-Co-O2-Zn configuration (O2, coordinated with two Co ions and one Zn ion) was found to be critical to regulating the OER mechanism (Fig. 12c, d). As expected, $\text{Zn}_{0.2}\text{Co}_{0.8}\text{OOH}$ with many Zn-O2-Co-O2-Zn local structures showed the highest specific activity of $0.38 \text{ mA cm}^{-2}_\text{ox}$ at a constant overpotential of 270 mV, which is about 38 times higher than unmodified CoOOH . In future, more catalysts based on LOM may be expected through this similar design principle. It must be shortly mentioned that the occurrence of the LOM is concurrent with the conventional AEM mechanism based on thermodynamic and kinetic considerations.^{149, 167} Kolpak and co-workers also demonstrated that both mechanisms are possible for oxides with a moderate metal-oxygen covalency, but LOM is favored as supported by DFT calculations.¹⁴⁹ Actually, the oxygen-containing intermediates adsorbed on oxide surface can be resulted from the electrolyte or from the lattice oxygen ions, which cannot be readily distinguishable during the OER process. This is because the oxygen vacancy after lattice oxygen release can be refilled by OH^- from the electrolyte. The understanding of the issue that which physicochemical properties of the catalysts determine the competition between AEM and LOM remains elusive. On the other hand, more experimental evidence should be provided to support the proposed reaction steps for LOM.



(b) Schematic formation of O_{NB} by extrapolating the molecular orbital energy diagram for octahedral MO_6 . (c) Free energies of OER steps via both mechanisms on CoO_2 and Zn-substituted CoO_2 , respectively. (d) Switching OER mechanism from AEM to LOM with the elimination of unoccupied oxygen states in $\text{Zn}_{0.2}\text{Co}_{0.8}\text{O}_2$. Reproduced from ref. 163 with permission from Macmillan Publishers Limited, Copyright 2019.

Fig. 12 (a) Model of Zn-substituted MO_2 (Purple, green and red balls represent M, Zn and O atoms, respectively.).

Table 1. Important design parameters and their representative electrocatalysts. (The catalysts listed from No. 1 to 19 follow AEM, whereas the catalysts listed from No. 20 to 23 follow LOM.)

NO.	Catalyst	Design parameter	Active site	Ref.
$\Delta G_{\text{O}^*} - \Delta G_{\text{H}_2\text{O}^*}$				
1	Ni-doped $\alpha\text{-Fe}_2\text{O}_3$	substitution of foreign elements	Fe	56
2	Gelled FeCoW oxyhydroxide	substitution of foreign elements	Co	78
3	$\text{CoO}(111)$	oxygen vacancies	Co	60
4	$\text{SnCo}_{0.9}\text{Fe}_{0.1}(\text{OH})_6$	Sn vacancies	Co	59
5	LaNiO_3	compressive strain	Ni	63
6	LaCoO_3	tensile strain	Co	65
7	Ce- NiO_x/Au	interface	Ni-edge	68
e_g orbital occupancy				
8	$\text{CaMnO}_{2.5}$	oxidation state	$\text{Mn}^{3+}(e_g=1)$	79
9	$\text{LaCoO}_3(100)$ film	spin state	$\text{Co}^{3+}(e_g=1)$	115
10	LaCoO_3 nanoparticle	spin state	$\text{Co}^{3+}(e_g=1)$	117
11	Fe-doped LaCoO_3	spin state	$\text{Co}^{3+}(e_g=1)$	114
Metal-oxygen covalency				
12	LaNiO_3	$\text{hole}_{e_g} + 1/4\text{hole}_{t_{2g}}$	Ni-O	90
13	$\text{Ba}_{0.5}\text{Sr}_{0.5}\text{Co}_{0.8}\text{Fe}_{0.2}\text{O}_{3-\delta}$	O p -band center	Co	96
14	Fe-substituted ZnCo_2O_4	charge-transfer energy	Co_{OCT}	123

15	$\text{Li}_{0.5}\text{Zn}_{0.5}\text{Fe}_{0.125}\text{Co}_{1.875}\text{O}_4$	O-charge	Co_{oct}	124
Stabilizing of HOO* independent on HO*				
16	Ni-NHGFs	Dual-site mechanism	NiN_4C_4 moieties	127
17	Confined RuO_2	Formation of hydrogen bond	$\text{Ru}(*\text{OOH}\cdots\text{O}_b)$ (0.2 eV)	128
18	$\text{La}_{0.5}\text{Sr}_{0.5}\text{CoO}_{3-\delta}$ functionalized by Pi	Introduction of proton acceptor	$\text{Co}(*\text{OO}) + \text{Pi}(*\text{H})$	135
19	$\text{Sr}(\text{Co}_{0.8}\text{Fe}_{0.2})_{0.7}\text{B}_{0.3}\text{O}_{3-\delta}$	Introduction of proton acceptor	$\text{Co/Fe}(*\text{OO}) + \text{Sr}_3\text{B}_2\text{O}_6(*\text{H})$	136
Activating lattice oxygen oxidation				
20	$\text{SrCoO}_{3-\delta}$	charge-transfer energy	O	143
21	LaNiO_3	N-V	O	148
22	$\text{La}_{0.5}\text{Sr}_{1.5}\text{Ni}_{0.7}\text{Fe}_{0.3}\text{O}_{4\pm\delta}$	cross-gap hybridization	O	150
23	$\text{Zn}_{0.2}\text{Co}_{0.8}\text{OOH}$	oxygen holes along Zn-O2-Co- O2-Zn configuration	O	163

4. Conclusions and perspectives

The development of efficient and low-cost OER catalysts has been one of the most active research areas of chemistry and materials in recent years. Understanding OER mechanism is the prerequisite to the rational design of better catalysts. In this review, we have summarized the different mechanisms and corresponding strategies to improve the OER activity of heterogeneous transition-metal based catalysts. Important design parameters and their representative electrocatalysts are summarized in Table 1. However, developing low-cost OER catalysts for practical applications with high activity and stability remains a great challenge. More efforts are necessary to be made according to the following aspects:

4.1 Improving intrinsic activity beyond the scaling relation. Nørskov and coworkers recently pointed out that the electrocatalytic OER activity has been improved slightly in the past decade, presumably due to the existence of the scaling relation between HO^* and HOO^* .¹²⁶ Novel catalyst design strategies are needed such that the stability of different intermediates can be varied independently. Some strategies to break this scaling relation have been proposed, including stabilization of HOO^* independent on HO^* , introduction of proton acceptor, and activation of LOM. Breaking the scaling relation of HOO^* and HO^* sometimes may not lead to the improved activity due to the possible ill-suited adsorption energies of intermediates.¹⁶⁸⁻¹⁷⁰ Future efforts directed to the design of enhanced OER catalysts may focus not only on breaking the HOO^* and HO^* scaling relation, but also on optimizing the free energy barrier of every OER step to approach the equilibrium potential of 1.23 eV. It will be challenging to synthesize the targeted OER catalysts with both features of breaking the HOO^* and HO^* scaling and optimizing adsorption energies of various intermediates independently.

4.2 Advanced tools for *in-situ* observation. The direct experimental evidence for the proposed OER mechanisms and active sites is still limited owing to the difficulty in detecting the intermediates and their adsorption behaviors. Particularly, the lattice oxygen exchange reaction, has already been found as early as many decades ago but now an increasing number of experimental evidences and theoretical calculations support this reaction pathway. It is still a great challenge to understand and control the competition between different

reaction mechanisms corresponding to redox chemistry of metal and oxygen on the surface of complex oxides. Different characterization methods have different cell configurations. Currently, there is no technique that can capture a complete overview of phase transformations, valence state changes, morphological variations, etc. under OER conditions. Motivated by these challenges, more *in-situ* characterization techniques such as femtosecond spectra, near atmospheric X-ray photoelectron spectra (NAP-XPS), near atmospheric scanning tunneling microscopy (NAP-STM), *in-situ* X-ray absorption spectroscopy (XAS), *in situ* diffuse reflectance infrared Fourier transform (DRIFT) spectra, corroborated with DFT computations, etc., should be developed to capture reaction intermediates and to better understand the reaction mechanism and the behavior of the active sites.

4.3 Development of practical alkaline anion exchange membrane. Most of transition metal-based oxide catalysts can only survive in alkaline media. The hydroxide anions typically show the mobility and diffusion coefficients of 1.75 times lower than that of protons in aqueous solutions (hydroxide anions with a mobility of $20.64 \times 10^{-4} \text{ cm}^2 \text{ V}^{-1} \text{ s}^{-1}$ and a diffusion coefficient of $5.3 \times 10^{-5} \text{ cm}^2 \text{ s}^{-1}$ vs. protons with a mobility of $36.23 \times 10^{-4} \text{ cm}^2 \text{ V}^{-1} \text{ s}^{-1}$ and a diffusion coefficient of $9.3 \times 10^{-5} \text{ cm}^2 \text{ s}^{-1}$).¹⁷¹ In a polymer electrolyte (anion exchange membrane (AEM)), the mobility of anions can be even lower. Even worse, the hydroxide anions can be easily converted to other anions by the dissolved contamination, such as CO_2 . Under this circumstance, the conductivity of AEM will be further reduced. On the other hand, the poor chemical stability of current developed AEMs is another concern. Hence, the verification of activity and stability of these electrocatalysts by a membrane electrode assembly (MEA) configuration is still a greater challenge. A conductive and durable AEM is highly desired for benchmarking the performance of transition metal-based oxide catalysts at a MEA level.¹⁷²

4.4 Development of acid-stable electrocatalysts. With regarding to the state-of-the-art technique of membranes, the proton exchange membrane (PEM) electrolyzer is more promising for water electrolysis. PEM creates a locally acidic environment (the acidity of

Nafion is about 1 M proton), but most transition metal-based oxides cannot survive in acidic environment. To date, the only acid-stable catalyst with sufficiently high activity are the Ir-based oxides, but Ir is one of the scarcest elements in the Earth's crust.^{35, 173-176} Actually, the benchmark IrO₂ in alkaline and acid media also face the same dissolution problem owing to the formation of water-soluble IrO₄²⁻ anion.^{141, 177} For the practical application, it is thus highly imperative to develop nonprecious OER catalysts that are efficient and stable under acid condition, which should be a great challenge. Recently, Li and co-workers reported an acid-stable catalyst of γ -MnO₂, which shows negligible deactivation even after electrolysis for 8000 h at a pH of 2.¹⁷⁸ This work indicates that exploring the suitable potential window for the transition metal oxides to work in acid is necessary. Additionally, the incorporation of heteroatom atoms such as Ti and Ge into MnO₂ could effectively stabilize the reaction termination with more undercoordinated sites on MnO₂, which opens up the possibility for surface engineering to develop nonprecious catalysts operated in acid electrolytes for a long time.^{179, 180}

4.5 Reconstruction mechanism of electrocatalysts: Metal chalcogenides, pnictides, and carbides have become exciting new classes of OER catalysts due to their reported high activity.^{181, 182} However, their composition and structure may not represent the catalyst under OER conditions, called the pre-catalyst. This is because they can be either completely oxidized, left unoxidized, or transformed into core@shell particles under OER conditions. Therefore, more thorough nanoscale chemical analysis are required to determine the real active phase for these catalysts. It is especially critical in explaining the observed enhancement in performance after long-term electrolysis. In addition, stainless steel has also been exploited for OER due to the presence of nonnegligible proportion of transition metal components (such as Ni, Mn, Co, Fe).¹⁸³⁻¹⁸⁷ It has been found highly active towards OER experimentally. Under the OER condition, the surface transformation to oxides and oxyhydroxides should happen due to the oxidation of these metals, which should be the active phase for OER.¹⁸⁸ It deserves a detailed study in terms of surface chemistry, intrinsic activity, and stability. Metal oxides can be reconstructed dynamically under OER conditions, too.¹⁸⁸ For example, within the OER potential region, the sub-nanometre shell of Co₃O₄ is found to be transformed into amorphous CoO_x(OH)_y that is composed of di- μ -oxobridged Co^{3+/4+} ions.^{189, 190} Impressively, the formed catalytically active layer is reversed back to the original state when returning to non-OER potential region. Different from this, highly reactive Ir-based catalysts give irreversible surface amorphization. The resulting surface is composed of short-range ordered octahedral IrO_xH_y phase regardless of the starting structure or composition of the catalysts.^{173, 175} Some highly covalent late transition metal oxides such as Ba_{0.5}Sr_{0.5}Co_{0.8}Fe_{0.2}O_{3- δ} (BSCF) and ZnCo_{1-x}Ni_xO₄ also go for LOM-driven self-reconstruction to form amorphous oxyhydroxides at the surface as the real catalytic species for OER.^{41, 191, 192} The metal ions like Ba²⁺ and Sr²⁺ with higher solubility in alkaline solution are prone to leach out from the oxide surface, while the transition metal ions with lower solubility remain on the surface to form oxyhydroxide layer. However, the fundamental origin of the self-reconstruction of catalysts during electrocatalysis and the factors governing the self-reconstruction and catalytic performance are not fully understood. Therefore, to better design the targeted catalysts, the researchers should pay more attention to the mechanism of reconstruction of OER (pre-)catalysts.

4.6 Further efforts to clarify the details behind the electrode-

electrolyte interface. Electrocatalytic reactions take place at the electrode-electrolyte interface. Efforts should be given to explore the nature of interactions between covalently bonded adsorbates and non-covalent forces in the double electric layer.¹⁹³⁻¹⁹⁵ Current challenges mainly include the depictions of solvent and ion near the interface at atomic and molecular level, and the kinetics and reaction barriers of key elementary steps involving proton and electron transfers during OER process. As the frontier of electrocatalysis research, more advanced methods are needed in both theory and experiment to clarify the details behind the electrode-electrolyte interface that link to the activity. This will further guide the community to develop better catalysts.

4.7 Development of water electrolyzers. Recently, Jaramillo and co-workers have successfully translated a low-cost, non-precious metal cobalt phosphide catalyst from 1 cm² lab-scale experiments to a large-scale (86 cm²) polymer membrane electrolyte electrolyzer.⁵ Looking beyond academic interest, the newly developed non-precious OER catalysts have not been successfully applied in a commercial device. The operating conditions of the actual devices often pose more stringent constraints on the selection of materials. For example, alkaline electrolyzers typically work at high temperatures (70-100°C), pressures (>10 bar), and electrolyte concentrations (>1 M KOH) to achieve an appreciable energy efficiency.¹⁹⁶ Under these harsh conditions, the stability of catalysts has yet been systematically studied. The characterization of catalysts before and after reaction can provide an initial understanding of catalyst degradation and will establish the knowledge base for all newly developed catalysts. A fundamental understanding of the degradation mechanism still needs to be strengthened. It is also a challenge to maintain the strong adhesion between catalyst layers and the current collectors under the operation conditions. More importantly, the synthesis and integration of catalyst should adapt to the manufacturing technology of electrolyzers, and meet the fundamental economical and scaling requirements simultaneously. The combination of semiconductor photocatalyst with these developed electrocatalysts to construct the photoelectrocatalytic (PEC) water splitting device is another promising direction to directly utilize the solar energy.¹⁹⁷⁻¹⁹⁹

Conflicts of interest

There are no conflicts to declare.

Acknowledgements

This work was supported by the Campus for Research Excellence and Technological Enterprise (CREATE) in Singapore and the Singapore Ministry of Education Tier 2 Grants (MOE2017-T2-1-009 and MOE2018-T2-2-027 (S)) and Tier 1 Grant (RG3/18 (S)).

Notes and references

1. S. Chu and A. Majumdar, *Nature*, 2012, **488**, 294-303.
2. T. J. Meyer, *Nature*, 2008, **451**, 778-779.
3. J. A. Turner, *Science*, 1999, **285**, 687-689.
4. Z. F. Huang, J. Song, L. Pan, X. Zhang, L. Wang and J. J. Zou, *Adv. Mater.*, 2015, **27**, 5309-5327.

5. L. A. King, M. A. Hubert, C. Capuano, J. Manco, N. Danilovic, E. Valle, T. R. Hellstern, K. Ayers and T. F. Jaramillo, *Nat. Nanotechnol.*, 2019, DOI: 10.1038/s41565-019-0550-7.
6. J. Kibsgaard and I. Chorkendorff, *Nat. Energy*, 2019, **4**, 430-433.
7. B. You and Y. Sun, *Acc. Chem. Res.*, 2018, **51**, 1571-1580.
8. L. Zhang, M. Zhou, A. Wang and T. Zhang, *Chem. Rev.*, 2019, DOI: 10.1021/acs.chemrev.9b00230.
9. J. Song, Z.-F. Huang, L. Pan, K. Li, X. Zhang, L. Wang and J.-J. Zou, *Appl. Catal. B*, 2018, **227**, 386-408.
10. J. H. Montoya, L. C. Seitz, P. Chakthranont, A. Vojvodic, T. F. Jaramillo and J. K. Nørskov, *Nat. Mater.*, 2016, **16**, 70-81.
11. C. Wei, R. R. Rao, J. Peng, B. Huang, I. E. L. Stephens, M. Risch, Z. J. Xu and Y. Shao-Horn, *Adv. Mater.*, 2019, **31**, e1806296.
12. C. C. McCrory, S. Jung, J. C. Peters and T. F. Jaramillo, *J. Am. Chem. Soc.*, 2013, **135**, 16977-16987.
13. Y. Lee, J. Suntivich, K. J. May, E. E. Perry and Y. Shao-Horn, *J. Phys. Chem. Lett.*, 2012, **3**, 399-404.
14. Q. Shi, C. Zhu, D. Du and Y. Lin, *Chem. Soc. Rev.*, 2019, **48**, 3181-3192.
15. L. Han, S. Dong and E. Wang, *Adv. Mater.*, 2016, **28**, 9266-9291.
16. B. M. Hunter, H. B. Gray and A. M. Muller, *Chem. Rev.*, 2016, **116**, 14120-14136.
17. N. T. Suen, S. F. Hung, Q. Quan, N. Zhang, Y. J. Xu and H. M. Chen, *Chem. Soc. Rev.*, 2017, **46**, 337-365.
18. S. Anantharaj and V. Aravindan, *Adv. Energy. Mater.*, 2019, **10**, 1902666.
19. C. Wei, S. Sun, D. Mandler, X. Wang, S. Z. Qiao and Z. J. Xu, *Chem. Soc. Rev.*, 2019, **48**, 2518-2534.
20. S. Sun, H. Li and Z. J. Xu, *Joule*, 2018, **2**, 1024-1027.
21. C. Wei and Z. J. Xu, *Small Methods*, 2018, **2**, 1800168.
22. H. Wang, H. W. Lee, Y. Deng, Z. Lu, P. C. Hsu, Y. Liu, D. Lin and Y. Cui, *Nat. Commun.*, 2015, **6**, 7261.
23. B. Y. Xia, Y. Yan, N. Li, H. B. Wu, X. W. Lou and X. Wang, *Nat. Energy*, 2016, **1**, 15006.
24. L. Han, X. Y. Yu and X. W. Lou, *Adv. Mater.*, 2016, **28**, 4601-4605.
25. J. Bao, X. Zhang, B. Fan, J. Zhang, M. Zhou, W. Yang, X. Hu, H. Wang, B. Pan and Y. Xie, *Angew. Chem. Int. Ed.*, 2015, **54**, 7399-7404.
26. X. Gao, H. Zhang, Q. Li, X. Yu, Z. Hong, X. Zhang, C. Liang and Z. Lin, *Angew. Chem. Int. Ed.*, 2016, **55**, 6290-6294.
27. L. Yu, J. F. Yang, B. Y. Guan, Y. Lu and X. W. D. Lou, *Angew. Chem. Int. Ed.*, 2018, **57**, 172-176.
28. F. Song and X. Hu, *Nat. Commun.*, 2014, **5**, 4477.
29. X. F. Lu, L. F. Gu, J. W. Wang, J. X. Wu, P. Q. Liao and G. R. Li, *Adv. Mater.*, 2017, **29**.
30. Y. Li, P. Hasin and Y. Wu, *Adv. Mater.*, 2010, **22**, 1926-1929.
31. Y. P. Zhu, C. Guo, Y. Zheng and S. Z. Qiao, *Acc. Chem. Res.*, 2017, **50**, 915-923.
32. B. M. Tackett, W. Sheng and J. G. Chen, *Joule*, 2017, **1**, 253-263.
33. X. Ma, Y. Shi, K. Wang, Y. Yu and B. Zhang, *Chem. Euro. J.*, 2019, DOI: 10.1002/chem.201904021.
34. T. Wu, S. Sun, J. Song, S. Xi, Y. Du, B. Chen, W. A. Sasangka, H. Liao, C. L. Gan, G. G. Scherer, L. Zeng, H. Wang, H. Li, A. Grimaud and Z. J. Xu, *Nat. Catal.*, 2019, **2**, 763-772.
35. Y. Chen, H. Li, J. Wang, Y. Du, S. Xi, Y. Sun, M. Sherburne, J. W. Ager III, A. C. Fisher and Z. J. Xu, *Nat. Commun.*, 2019, **10**, 572.
36. X. Xu, F. Song and X. Hu, *Nat. Commun.*, 2016, **7**, 12324.
37. C. W. Tung, Y. Y. Hsu, Y. P. Shen, Y. Zheng, T. S. Chan, H. S. Sheu, Y. C. Cheng and H. M. Chen, *Nat. Commun.*, 2015, **6**, 8106.
38. J. Duan, S. Chen and C. Zhao, *Nat. Commun.*, 2017, **8**, 15341.
39. C. Walter, P. W. Menezes, S. Orthmann, J. Schuch, P. Connor, B. Kaiser, M. Lerch and M. Driess, *Angew. Chem. Int. Ed.*, 2018, **57**, 698-702.
40. F. Hu, S. Zhu, S. Chen, Y. Li, L. Ma, T. Wu, Y. Zhang, C. Wang, C. Liu, X. Yang, L. Song, X. Yang and Y. Xiong, *Adv. Mater.*, 2017, **29**, 1606570.
41. E. Fabbri, M. Nachtegaal, T. Binninger, X. Cheng, B. J. Kim, J. Durst, F. Bozza, T. Graule, R. Schaublin, L. Wiles, M. Pertoso, N. Danilovic, K. E. Ayers and T. J. Schmidt, *Nat. Mater.*, 2017, **16**, 925-931.
42. B. Han, K. A. Stoerzinger, V. Tileli, A. D. Gamalski, E. A. Stach and Y. Shao-Horn, *Nat. Mater.*, 2017, **16**, 121-126.
43. C. Niether, S. Faure, A. Bordet, J. Deseure, M. Chatenet, J. Carrey, B. Chaudret and A. Rouet, *Nat. Energy*, 2018, **3**, 476-483.
44. Y. Zhu, G. Chen, Y. Zhong, Y. Chen, N. Ma, W. Zhou and Z. Shao, *Nat. Commun.*, 2018, **9**, 2326.
45. I. C. Man, H. Y. Su, F. Calle - Vallejo, H. A. Hansen, J. I. Martínez, N. G. Inoglu, J. Kitchin, T. F. Jaramillo, J. K. Nørskov and J. Rossmeisl, *ChemCatChem*, 2011, **3**, 1159-1165.
46. J. Rossmeisl, A. Logadottir and J. K. Nørskov, *Chem. Phys.*, 2005, **319**, 178-184.
47. J. Rossmeisl, Z. W. Qu, H. Zhu, G. J. Kroes and J. K. Nørskov, *J. Electroanal. Chem.*, 2007, **607**, 83-89.
48. J. K. Nørskov, J. Rossmeisl, A. Logadottir, L. Lindqvist, J. R. Kitchin, T. Bligaard and H. Jónsson, *J. Phys. Chem. B*, 2004, **108**, 17886-17892.
49. Z. F. Huang, J. Song, K. Li, M. Tahir, Y. T. Wang, L. Pan, L. Wang, X. Zhang and J. J. Zou, *J. Am. Chem. Soc.*, 2016, **138**, 1359-1365.
50. H. Dau, C. Limberg, T. Reier, M. Risch, S. Roggan and P. Strasser, *ChemCatChem*, 2010, **2**, 724-761.
51. M. Bajdich, M. Garcia-Mota, A. Vojvodic, J. K. Nørskov and A. T. Bell, *J. Am. Chem. Soc.*, 2013, **135**, 13521-13530.
52. O. Diaz-Morales, I. Ledezma-Yanez, M. T. M. Koper and F. Calle-Vallejo, *ACS Catal.*, 2015, **5**, 5380-5387.
53. K. Fan, H. Chen, Y. Ji, H. Huang, P. M. Claesson, Q. Daniel, B. Philippe, H. Rensmo, F. Li, Y. Luo and L. Sun, *Nat. Commun.*, 2016, **7**, 11981.
54. J. Feng, F. Lv, W. Zhang, P. Li, K. Wang, C. Yang, B. Wang, Y. Yang, J. Zhou, F. Lin, G. C. Wang and S. Guo, *Adv. Mater.*, 2017, **29**, 1703798.
55. J. Jiang, F. Sun, S. Zhou, W. Hu, H. Zhang, J. Dong, Z. Jiang, J. Zhao, J. Li, W. Yan and M. Wang, *Nat. Commun.*, 2018, **9**, 2885.
56. P. Liao, J. A. Keith and E. A. Carter, *J. Am. Chem. Soc.*, 2012, **134**, 13296-13309.
57. J. Liu, Y. Ji, J. Nai, X. Niu, Y. Luo, L. Guo and S. Yang, *Energy Environ. Sci.*, 2018, **11**, 1736-1741.
58. S. H. Ye, Z. X. Shi, J. X. Feng, Y. X. Tong and G. R. Li, *Angew. Chem. Int. Ed.*, 2018, **57**, 2672-2676.
59. D. Chen, M. Qiao, Y. R. Lu, L. Hao, D. Liu, C. L. Dong, Y. Li and S. Wang, *Angew. Chem. Int. Ed.*, 2018, **57**, 8691-8696.
60. T. Ling, D. Y. Yan, Y. Jiao, H. Wang, Y. Zheng, X. Zheng, J. Mao, X. W. Du, Z. Hu, M. Jaroniec and S. Z. Qiao, *Nat. Commun.*, 2016, **7**, 12876.
61. M.-T. Nguyen, S. Piccinin, N. Seriani and R. Gebauer, *ACS Catal.*, 2014, **5**, 715-721.
62. L. Zhuang, L. Ge, Y. Yang, M. Li, Y. Jia, X. Yao and Z. Zhu, *Adv. Mater.*, 2017, **29**.
63. J. R. Petrie, V. R. Cooper, J. W. Freeland, T. L. Meyer, Z. Zhang, D. A. Lutterman and H. N. Lee, *J. Am. Chem. Soc.*, 2016, **138**, 2488-2491.
64. J. M. Rondinelli and N. A. Spaldin, *Phys. Rev. B*, 2009, **79**, 054409.

65. K. A. Stoerzinger, W. S. Choi, H. Jeon, H. N. Lee and Y. Shao-Horn, *J. Phys. Chem. Lett.*, 2015, **6**, 487-492.
66. Z. Zhuang, W. Sheng and Y. Yan, *Adv. Mater.*, 2014, **26**, 3950-3955.
67. C. Guo, Y. Zheng, J. Ran, F. Xie, M. Jaroniec and S. Z. Qiao, *Angew. Chem. Int. Ed.*, 2017, **56**, 8539-8543.
68. J. W. D. Ng, M. García-Melchor, M. Bajdich, P. Chakthranont, C. Kirk, A. Vojvodic and T. F. Jaramillo, *Nat. Energy*, 2016, **1**, 16053.
69. L. C. Seitz, C. F. Dickens, K. Nishio, Y. Hikita, J. Montoya, A. Doyle, C. Kirk, A. Vojvodic, H. Y. Hwang, J. K. Nørskov and T. F. Jaramillo, *Science*, 2016, **353**, 1011-1014.
70. J. Wang, K. Li, H. X. Zhong, D. Xu, Z. L. Wang, Z. Jiang, Z. J. Wu and X. B. Zhang, *Angew. Chem. Int. Ed.*, 2015, **54**, 10530-10534.
71. L. Trotochaud, S. L. Young, J. K. Ranney and S. W. Boettcher, *J. Am. Chem. Soc.*, 2014, **136**, 6744-6753.
72. J. A. Haber, Y. Cai, S. Jung, C. Xiang, S. Mitrovic, J. Jin, A. T. Bell and J. M. Gregoire, *Energy Environ. Sci.*, 2014, **7**, 682-688.
73. J. A. Haber, E. Anzenburg, J. Yano, C. Kisielowski and J. M. Gregoire, *Adv. Energy. Mater.*, 2015, **5**, 1402307.
74. Y. Pi, Q. Shao, P. Wang, F. Lv, S. Guo, J. Guo and X. Huang, *Angew. Chem. Int. Ed.*, 2017, **56**, 4502-4506.
75. E. Detsi, J. B. Cook, B. Lesel, C. Turner, Y. L. Liang, S. Robbenolt and S. H. Tolbert, *Energy Environ. Sci.*, 2016, **9**, 540-549.
76. J. B. Gerken, S. E. Shaner, R. C. Massé, N. J. Porubsky and S. S. Stahl, *Energy Environ. Sci.*, 2014, **7**, 2376-2382.
77. C. Schwanke, H. S. Stein, L. Xi, K. Sliozberg, W. Schuhmann, A. Ludwig and K. M. Lange, *Sci. Rep.*, 2017, **7**, 44192.
78. B. Zhang, X. Zheng, O. Voznyy, R. Comin, M. Bajdich, M. Garcia-Melchor, L. Han, J. Xu, M. Liu, L. Zheng, F. P. Garcia de Arquer, C. T. Dinh, F. Fan, M. Yuan, E. Yassitepe, N. Chen, T. Regier, P. Liu, Y. Li, P. De Luna, A. Janmohamed, H. L. Xin, H. Yang, A. Vojvodic and E. H. Sargent, *Science*, 2016, **352**, 333-337.
79. J. Kim, X. Yin, K. C. Tsao, S. Fang and H. Yang, *J. Am. Chem. Soc.*, 2014, **136**, 14646-14649.
80. L. Xu, Q. Jiang, Z. Xiao, X. Li, J. Huo, S. Wang and L. Dai, *Angew. Chem. Int. Ed.*, 2016, **55**, 5277-5281.
81. Y. Jia, K. Jiang, H. Wang and X. Yao, *Chem*, 2019, **5**, 1371-1397.
82. C. Xie, D. Yan, W. Chen, Y. Zou, R. Chen, S. Zang, Y. Wang, X. Yao and S. Wang, *Mater. Today*, 2019, DOI: 10.1016/j.mattod.2019.05.021.
83. L. Pan, S. Wang, W. Mi, J. Song, J.-J. Zou, L. Wang and X. Zhang, *Nano Energy*, 2014, **9**, 71-79.
84. S. Wang, L. Pan, J. J. Song, W. Mi, J. J. Zou, L. Wang and X. Zhang, *J. Am. Chem. Soc.*, 2015, **137**, 2975-2983.
85. J. Hwang, Z. Feng, N. Charles, X. R. Wang, D. Lee, K. A. Stoerzinger, S. Muy, R. R. Rao, D. Lee, R. Jacobs, D. Morgan and Y. Shao-Horn, *Mater. Today*, 2019, DOI: doi.org/10.1016/j.mattod.2019.03.014.
86. Y. Zang, S. Niu, Y. Wu, X. Zheng, J. Cai, J. Ye, Y. Xie, Y. Liu, J. Zhou, J. Zhu, X. Liu, G. Wang and Y. Qian, *Nat. Commun.*, 2019, **10**, 1217.
87. L. Wang, Z. Zeng, W. Gao, T. Maxson, D. Raciti, M. Giroux, X. Pan, C. Wang and J. Greeley, *Science*, 2019, **363**, 870-874.
88. R. Xiang, L. Peng and Z. Wei, *Chem. Euro. J.*, 2019, **25**, 9799-9815.
89. W. T. Hong, R. E. Welsch and Y. Shao-Horn, *J. Phys. Chem. C*, 2015, **120**, 78-86.
90. J. Suntivich, K. J. May, H. A. Gasteiger, J. B. Goodenough and Y. Shao-Horn, *Science*, 2011, **334**, 1383-1385.
91. C. Wei, Z. Feng, G. G. Scherer, J. Barber, Y. Shao-Horn and Z. J. Xu, *Adv. Mater.*, 2017, **29**, 1606800.
92. A. Vojvodic and J. K. Nørskov, *Science*, 2011, **334**, 1355-1356.
93. R. Subbaraman, D. Tripkovic, K. C. Chang, D. Strmcnik, A. P. Paulikas, P. Hirunsit, M. Chan, J. Greeley, V. Stamenkovic and N. M. Markovic, *Nat. Mater.*, 2012, **11**, 550-557.
94. B. Hammer and J. K. Nørskov, *Advances in Catalysis*, 2000, **45**, 71-129.
95. F. Cheng, J. Shen, B. Peng, Y. Pan, Z. Tao and J. Chen, *Nat. Chem.*, 2011, **3**, 79-84.
96. A. Grimaud, K. J. May, C. E. Carlton, Y. L. Lee, M. Risch, W. T. Hong, J. Zhou and Y. Shao-Horn, *Nat. Commun.*, 2013, **4**, 2439.
97. F. Calle-Vallejo, N. G. Inoglu, H.-Y. Su, J. I. Martínez, I. C. Man, M. T. M. Koper, J. R. Kitchin and J. Rossmeisl, *Chem. Sci.*, 2013, **4**, 1245.
98. F. Calle-Vallejo, O. A. Díaz-Morales, M. J. Kolb and M. T. M. Koper, *ACS Catal.*, 2015, **5**, 869-873.
99. H. B. Tao, L. Fang, J. Chen, H. B. Yang, J. Gao, J. Miao, S. Chen and B. Liu, *J. Am. Chem. Soc.*, 2016, **138**, 9978-9985.
100. H. Li, S. Sun, S. Xi, Y. Chen, T. Wang, Y. Du, M. Sherburne, J. W. Ager, A. C. Fisher and Z. J. Xu, *Chem. Mater.*, 2018, **30**, 6839-6848.
101. H. Li, Y. Chen, S. Xi, J. Wang, S. Sun, Y. Sun, Y. Du and Z. J. Xu, *Chem. Mater.*, 2018, **30**, 4313-4320.
102. W. T. Hong, K. A. Stoerzinger, Y.-L. Lee, L. Giordano, A. Grimaud, A. M. Johnson, J. Hwang, E. J. Crumlin, W. Yang and Y. Shao-Horn, *Energy Environ. Sci.*, 2017, **10**, 2190-2200.
103. T. Lim, J. W. Niemantsverdriet and J. Gracia, *ChemCatChem*, 2016, **8**, 2968-2974.
104. R. R. Chen, Y. Sun, S. J. H. Ong, S. Xi, Y. Du, C. Liu, O. Lev and Z. J. Xu, *Adv. Mater.*, 2020, DOI: 10.1002/adma.201907976.
105. S. Sun, Y. Sun, Y. Zhou, J. Shen, D. Mandler, R. Neumann and Z. J. Xu, *Chem. Mater.*, 2019, **31**, 8106-8111.
106. W. T. Hong, M. Risch, K. A. Stoerzinger, A. Grimaud, J. Suntivich and Y. Shao-Horn, *Energy Environ. Sci.*, 2015, **8**, 1404-1427.
107. Y. Guo, Y. Tong, P. Chen, K. Xu, J. Zhao, Y. Lin, W. Chu, Z. Peng, C. Wu and Y. Xie, *Adv. Mater.*, 2015, **27**, 5989-5994.
108. J. G. Lee, J. Hwang, H. J. Hwang, O. S. Jeon, J. Jang, O. Kwon, Y. Lee, B. Han and Y. G. Shul, *J. Am. Chem. Soc.*, 2016, **138**, 3541-3547.
109. Y. Zhou, S. Sun, S. Xi, Y. Duan, T. Sritharan, Y. Du and Z. J. Xu, *Adv. Mater.*, 2018, **30**, 1705407.
110. B. Zhao, L. Zhang, D. Zhen, S. Yoo, Y. Ding, D. Chen, Y. Chen, Q. Zhang, B. Doyle, X. Xiong and M. Liu, *Nat. Commun.*, 2017, **8**, 14586.
111. Y. Zhao, X. Jia, G. Chen, L. Shang, G. I. Waterhouse, L. Z. Wu, C. H. Tung, D. O'Hare and T. Zhang, *J. Am. Chem. Soc.*, 2016, **138**, 6517-6524.
112. J. Huang, J. Chen, T. Yao, J. He, S. Jiang, Z. Sun, Q. Liu, W. Cheng, F. Hu, Y. Jiang, Z. Pan and S. Wei, *Angew. Chem. Int. Ed.*, 2015, **54**, 8722-8727.
113. Y. Zhu, W. Zhou, J. Yu, Y. Chen, M. Liu and Z. Shao, *Chem. Mater.*, 2016, **28**, 1691-1697.
114. Y. Duan, S. Sun, S. Xi, X. Ren, Y. Zhou, G. Zhang, H. Yang, Y. Du and Z. J. Xu, *Chem. Mater.*, 2017, **29**, 10534-10541.
115. Y. Tong, Y. Guo, P. Chen, H. Liu, M. Zhang, L. Zhang, W. Yan, W. Chu, C. Wu and Y. Xie, *Chem*, 2017, **3**, 812-821.
116. J. Hwang, R. R. Rao, L. Giordano, Y. Katayama, Y. Yu and Y. Shao-Horn, *Science*, 2017, **358**, 751-756.
117. S. Zhou, X. Miao, X. Zhao, C. Ma, Y. Qiu, Z. Hu, J. Zhao, L. Shi and J. Zeng, *Nat. Commun.*, 2016, **7**, 11510.
118. D. V. Karpinsky, I. O. Troyanchuk, K. Bärner, H. Szymczak and M. Tovar, *J. Phys.: Condens. Matter*, 2005, **17**, 7219-7226.

119. S. Yagi, I. Yamada, H. Tsukasaki, A. Seno, M. Murakami, H. Fujii, H. Chen, N. Umezawa, H. Abe, N. Nishiyama and S. Mori, *Nat. Commun.*, 2015, **6**, 8249.
120. I. Yamada, A. Takamatsu, K. Asai, T. Shirakawa, H. Ohzuku, A. Seno, T. Uchimura, H. Fujii, S. Kawaguchi, K. Wada, H. Ikeno and S. Yagi, *J. Phys. Chem. C*, 2018, **122**, 27885-27892.
121. A. Grimaud, W. T. Hong, Y. Shao-Horn and J. M. Tarascon, *Nat. Mater.*, 2016, **15**, 121-126.
122. D. A. Kuznetsov, B. Han, Y. Yu, R. R. Rao, J. Hwang, Y. Román-Leshkov and Y. Shao-Horn, *Joule*, 2018, **2**, 225-244.
123. Y. Zhou, S. Sun, J. Song, S. Xi, B. Chen, Y. Du, A. C. Fisher, F. Cheng, X. Wang, H. Zhang and Z. J. Xu, *Adv. Mater.*, 2018, **30**, e1802912.
124. S. Sun, Y. Sun, Y. Zhou, S. Xi, X. Ren, B. Huang, H. Liao, L. P. Wang, Y. Du and Z. J. Xu, *Angew. Chem. Int. Ed.*, 2019, **58**, 6042-6047.
125. M. T. M. Koper, *Chem. Sci.*, 2013, **4**, 2710-2723.
126. A. Kulkarni, S. Siahrostami, A. Patel and J. K. Norskov, *Chem. Rev.*, 2018, **118**, 2302-2312.
127. H. Fei, J. Dong, Y. Feng, C. S. Allen, C. Wan, B. Voloskiy, M. Li, Z. Zhao, Y. Wang, H. Sun, P. An, W. Chen, Z. Guo, C. Lee, D. Chen, I. Shakir, M. Liu, T. Hu, Y. Li, A. I. Kirkland, X. Duan and Y. Huang, *Nat. Catal.*, 2018, **1**, 63-72.
128. A. D. Doyle, J. H. Montoya and A. Vojvodich, *ChemCatChem*, 2015, **7**, 738-742.
129. R. R. Rao, M. J. Kolb, N. B. Halck, A. F. Pedersen, A. Mehta, H. You, K. A. Stoerzinger, Z. Feng, H. A. Hansen, H. Zhou, L. Giordano, J. Rossmeisl, T. Vegge, I. Chorkendorff, I. E. L. Stephens and Y. Shao-Horn, *Energy Environ. Sci.*, 2017, **10**, 2626-2637.
130. R. Frydendal, M. Busch, N. B. Halck, E. A. Paoli, P. Krttil, I. Chorkendorff and J. Rossmeisl, *ChemCatChem*, 2015, **7**, 149-154.
131. H. H. Pham, M.-J. Cheng, H. Frei and L.-W. Wang, *ACS Catal.*, 2016, **6**, 5610-5617.
132. N. B. Halck, V. Petrykin, P. Krttil and J. Rossmeisl, *Phys. Chem. Chem. Phys.*, 2014, **16**, 13682-13688.
133. T. Qiu, B. Tu, D. Saldana-Greco and A. M. Rappe, *ACS Catal.*, 2018, **8**, 2218-2224.
134. F. Song, M. M. Busch, B. Lassalle-Kaiser, C. S. Hsu, E. Petkucheva, M. Bensimon, H. M. Chen, C. Corminboeuf and X. Hu, *ACS Cent. Sci.*, 2019, **5**, 558-568.
135. C. Yang, C. Laberty-Robert, D. Batuk, G. Cibi, A. V. Chadwick, V. Pimenta, W. Yin, L. Zhang, J. M. Tarascon and A. Grimaud, *J. Phys. Chem. Lett.*, 2017, **8**, 3466-3472.
136. S. She, Y. Zhu, Y. Chen, Q. Lu, W. Zhou and Z. Shao, *Adv. Energy Mater.*, 2019, **9**, 1900429.
137. J. Hessels, R. J. Detz, M. T. M. Koper and J. N. H. Reek, *Chemistry*, 2017, **23**, 16413-16418.
138. M. Okamura, M. Kondo, R. Kuga, Y. Kurashige, T. Yanai, S. Hayami, V. K. Praneeth, M. Yoshida, K. Yoneda, S. Kawata and S. Masaoka, *Nature*, 2016, **530**, 465-468.
139. M. G. Mavros, T. Tsuchimochi, T. Kowalczyk, A. Mclsaac, L. P. Wang and T. V. Voorhis, *Inorg. Chem.*, 2014, **53**, 6386-6397.
140. T. A. Betley, Q. Wu, T. Van Voorhis and D. G. Nocera, *Inorg. Chem.*, 2008, **47**, 1849-1861.
141. J. T. Mefford, X. Rong, A. M. Abakumov, W. G. Hardin, S. Dai, A. M. Kolpak, K. P. Johnston and K. J. Stevenson, *Nat. Commun.*, 2016, **7**, 11053.
142. X. Rong, J. Parolin and A. M. Kolpak, *ACS Catal.*, 2016, **6**, 1153-1158.
143. A. Grimaud, O. Diaz-Morales, B. Han, W. T. Hong, Y. L. Lee, L. Giordano, K. A. Stoerzinger, M. T. M. Koper and Y. Shao-Horn, *Nat. Chem.*, 2017, **9**, 457-465.
144. C. Roy, B. Sebok, S. B. Scott, E. M. Fiordaliso, J. E. Sørensen, A. Bodin, D. B. Trimarco, C. D. Damsgaard, P. C. K. Vesborg, O. Hansen, I. E. L. Stephens, J. Kibsgaard and I. Chorkendorff, *Nat. Catal.*, 2018, **1**, 820-829.
145. S. W. Boettcher, *Nat. Catal.*, 2018, **1**, 814-815.
146. O. Diaz-Morales, D. Ferrus-Suspedra and M. T. M. Koper, *Chem. Sci.*, 2016, **7**, 2639-2645.
147. L. Giordano, B. Han, M. Risch, W. T. Hong, R. R. Rao, K. A. Stoerzinger and Y. Shao-Horn, *Catal. Today*, 2016, **262**, 2-10.
148. J. S. Yoo, Y. Liu, X. Rong and A. M. Kolpak, *J. Phys. Chem. Lett.*, 2018, **9**, 1473-1479.
149. J. S. Yoo, X. Rong, Y. S. Liu and A. M. Kolpak, *ACS Catal.*, 2018, **8**, 4628-4636.
150. R. P. Forslund, W. G. Hardin, X. Rong, A. M. Abakumov, D. Filimonov, C. T. Alexander, J. T. Mefford, H. Iyer, A. M. Kolpak, K. P. Johnston and K. J. Stevenson, *Nat. Commun.*, 2018, **9**, 3150.
151. M. Wohlfahrt-Mehrens and J. Heitbaum, *J. Electroanal. Chem. Interfacial Electrochem.*, 1987, **237**, 251-260.
152. S. Fierro, T. Nagel, H. Baltruschat and C. Comninellis, *Electrochem. Commun.*, 2007, **9**, 1969-1974.
153. K. Macounova, M. Makarova and P. Krttil, *Electrochem. Commun.*, 2009, **11**, 1865-1868.
154. H. M. A. Amin and H. Baltruschat, *Phys. Chem. Chem. Phys.*, 2017, **19**, 25527-25536.
155. H. M. A. Amin, P. Konigshoven, M. Hegemann and H. Baltruschat, *Anal. Chem.*, 2019, **91**, 12653-12660.
156. D. B. Hibbert and C. R. Churchill, *J. Chem. Soc. Faraday Trans.*, 1984, **80**, 1965-1975.
157. Y. Surendranath, M. W. Kanan and D. G. Nocera, *J. Am. Chem. Soc.*, 2010, **132**, 16501-16509.
158. L.-P. Wang and T. Van Voorhis, *J. Phys. Chem. Lett.*, 2011, **2**, 2200-2204.
159. S. Lee, K. Banjac, M. Lingenfelder and X. Hu, *Angew. Chem. Int. Ed.*, 2019, **58**, 10295-10299.
160. O. Diaz-Morales, F. Calle-Vallejo, C. de Munck and M. T. M. Koper, *Chem. Sci.*, 2013, **4**, 2334-2343.
161. J. Willsau, O. Wolter and J. Heitbaum, *J. Electroanal. Chem. Interfacial Electrochem.*, 1985, **195**, 299-306.
162. K. A. Stoerzinger, O. Diaz-Morales, M. Kolb, R. R. Rao, R. Frydendal, L. Qiao, X. R. Wang, N. B. Halck, J. Rossmeisl, H. A. Hansen, T. Vegge, I. E. L. Stephens, M. T. M. Koper and Y. Shao-Horn, *ACS Energy Lett.*, 2017, **2**, 876-881.
163. Z.-F. Huang, J. Song, Y. Du, S. Xi, S. Dou, J. M. V. Nsanzimana, C. Wang, Z. J. Xu and X. Wang, *Nat. Energy*, 2019, **4**, 329-338.
164. D. H. Seo, J. Lee, A. Urban, R. Malik, S. Kang and G. Ceder, *Nat. Chem.*, 2016, **8**, 692-697.
165. G. Assat and J.-M. Tarascon, *Nat. Energy*, 2018, **3**, 373-386.
166. J. Lee, D. A. Kitchaev, D. H. Kwon, C. W. Lee, J. K. Papp, Y. S. Liu, Z. Lun, R. J. Clement, T. Shi, B. D. McCloskey, J. Guo, M. Balasubramanian and G. Ceder, *Nature*, 2018, **556**, 185-190.
167. T. Binninger, R. Mohamed, K. Waltar, E. Fabbri, P. Levecque, R. Kötz and T. J. Schmidt, *Sci. Rep.*, 2015, **5**, 12167.
168. N. Govindarajan, J. M. García-Lastra, E. J. Meijer and F. Calle-Vallejo, *Curr. Opin. Electrochem.*, 2018, **8**, 110-117.
169. Z.-J. Zhao, S. Liu, S. Zha, D. Cheng, F. Studt, G. Henkelman and J. Gong, *Nat. Rev. Mater.*, 2019, DOI: 10.1038/s41578-019-0152-x.
170. J. Pérez-Ramírez and N. López, *Nat. Catal.*, 2019, **2**, 971-976.

171. N. Ramaswamy and S. Mukerjee, *Chem. Rev.*, 2019, DOI: 10.1021/acs.chemrev.9b00157.
172. Y. Zhou, S. Sun, C. Wei, Y. Sun, P. Xi, Z. Feng and Z. J. Xu, *Adv. Mater.*, 2019, DOI: 10.1002/adma.201902509.
173. R. Zhang, N. Dubouis, M. Ben Osman, W. Yin, M. T. Sougrati, D. A. D. Corte, D. Giaume and A. Grimaud, *Angew. Chem. Int. Ed.*, 2019, **58**, 4571-4575.
174. L. Yang, G. Yu, X. Ai, W. Yan, H. Duan, W. Chen, X. Li, T. Wang, C. Zhang, X. Huang, J. S. Chen and X. Zou, *Nat. Commun.*, 2018, **9**, 5236.
175. S. Geiger, O. Kasian, M. Ledendecker, E. Pizzutilo, A. M. Mingers, W. T. Fu, O. Diaz-Morales, Z. Li, T. Oellers, L. Fruchter, A. Ludwig, K. J. J. Mayrhofer, M. T. M. Koper and S. Cherevko, *Nat. Catal.*, 2018, **1**, 508-515.
176. O. Diaz-Morales, S. Raaijman, R. Kortlever, P. J. Kooyman, T. Wezendonk, J. Gascon, W. T. Fu and M. T. Koper, *Nat. Commun.*, 2016, **7**, 12363.
177. T. Li, O. Kasian, S. Cherevko, S. Zhang, S. Geiger, C. Scheu, P. Felfer, D. Raabe, B. Gault and K. J. J. Mayrhofer, *Nat. Catal.*, 2018, **1**, 300-305.
178. A. Li, H. Ooka, N. Bonnet, T. Hayashi, Y. Sun, Q. Jiang, C. Li, H. Han and R. Nakamura, *Angew. Chem. Int. Ed.*, 2019, **58**, 5054-5058.
179. R. Frydendal, E. A. Paoli, I. Chorkendorff, J. Rossmeisl and I. E. L. Stephens, *Adv. Energy. Mater.*, 2015, **5**, 1500991.
180. T. Reier, H. N. Nong, D. Teschner, R. Schlögl and P. Strasser, *Adv. Energy. Mater.*, 2017, **7**, 1601275.
181. B. R. Wygant, K. Kawashima and C. B. Mullins, *ACS Energy Lett.*, 2018, 2956-2966.
182. C. Lei, S. Lyu, J. Si, B. Yang, Z. Li, L. Lei, Z. Wen, G. Wu and Y. Hou, *ChemCatChem*, 2019, **11**, 5855-5874.
183. H. Schäfer and M. Chatenet, *ACS Energy Lett.*, 2018, **3**, 574-591.
184. H. Schäfer, D. M. Chevrier, P. Zhang, J. Stangl, K. Müller-Buschbaum, J. D. Hardege, K. Kuepper, J. Wollschläger, U. Krupp, S. Dühnen, M. Steinhart, L. Walder, S. Sadaf and M. Schmidt, *Adv. Funct. Mater.*, 2016, **26**, 6402-6417.
185. H. Schäfer, S. M. Beladi-Mousavi, L. Walder, J. Wollschläger, O. Kuschel, S. Ichilman, S. Sadaf, M. Steinhart, K. Küpper and L. Schneider, *ACS Catal.*, 2015, **5**, 2671-2680.
186. H. Schäfer, S. Sadaf, L. Walder, K. Kuepper, S. Dinklage, J. Wollschläger, L. Schneider, M. Steinhart, J. Hardege and D. Daum, *Energy Environ. Sci.*, 2015, **8**, 2685-2697.
187. W. Han, K. Kuepper, P. Hou, W. Akram, H. Eickmeier, J. Hardege, M. Steinhart and H. Schäfer, *ChemSusChem*, 2018, **11**, 3661-3671.
188. Z. J. Xu, *Sci. China Mater.*, 2019, DOI: 10.1007/s40843-019-9588-5.
189. A. Bergmann, E. Martinez-Moreno, D. Teschner, P. Chernev, M. Gliech, J. F. de Araujo, T. Reier, H. Dau and P. Strasser, *Nat. Commun.*, 2015, **6**, 8625.
190. A. Bergmann, T. E. Jones, E. Martinez Moreno, D. Teschner, P. Chernev, M. Gliech, T. Reier, H. Dau and P. Strasser, *Nat. Catal.*, 2018, **1**, 711-719.
191. B. J. Kim, E. Fabbri, D. F. Abbott, X. Cheng, A. H. Clark, M. Nachtegaal, M. Borlaf, I. E. Castelli, T. Graule and T. J. Schmidt, *J. Am. Chem. Soc.*, 2019, **141**, 5231-5240.
192. Y. Duan, S. Sun, Y. Sun, S. Xi, X. Chi, Q. Zhang, X. Ren, J. Wang, S. J. H. Ong, Y. Du, L. Gu, A. Grimaud and Z. J. Xu, *Adv. Mater.*, 2019, **31**, e1807898.
193. V. R. Stamenkovic, D. Strmcnik, P. P. Lopes and N. M. Markovic, *Nat. Mater.*, 2016, **16**, 57-69.
194. I. Ledezma-Yanez, W. D. Z. Wallace, P. Sebastián-Pascual, V. Climent, J. M. Feliu and M. T. M. Koper, *Nat. Energy*, 2017, **2**, 17031.
195. P. Rodriguez, Y. Kwon and M. T. Koper, *Nat. Chem.*, 2011, **4**, 177-182.
196. F. Song, L. Bai, A. Moysiadou, S. Lee, C. Hu, L. Liardet and X. Hu, *J. Am. Chem. Soc.*, 2018, **140**, 7748-7759.
197. K. Sivula and R. van de Krol, *Nat. Rev. Mater.*, 2016, **1**.
198. I. Roger, M. A. Shipman and M. D. Symes, *Nat. Rev. Chem.*, 2017, **1**.
199. T. W. Kim and K. S. Choi, *Science*, 2014, **343**, 990-994.